T CELLS

T_{regs} in visceral adipose tissue up-regulate circadian-clock expression to promote fitness and enforce a diurnal rhythm of lipolysis

Tianli Xiao[1], P. Kent Langston[1], Andrés R. Muñoz-Rojas[1], Teshika Jayewickreme[1], Mitchell A. Lazar[2,3,4], Christophe Benoist[1,5], Diane Mathis[1,5]*

Regulatory T cells (T_{regs}) in nonlymphoid organs provide critical brakes on inflammation and regulate tissue homeostasis. Although so-called "tissue T_{regs}" are phenotypically and functionally diverse, serving to optimize their performance and survival, up-regulation of pathways related to circadian rhythms is a feature they share. Yet the diurnal regulation of T_{regs} and its consequences are controversial and poorly understood. Here, we profiled diurnal variations in visceral adipose tissue (VAT) and splenic T_{regs} in the presence and absence of core-clock genes. VAT, but not splenic, T_{regs} up-regulated their cell-intrinsic circadian program and exhibited diurnal variations in their activation and metabolic state. BMAL1 deficiency specifically in T_{regs} led to constitutive activation and poor oxidative metabolism in VAT, but not splenic, T_{regs}. Disruption of core-clock components resulted in loss of fitness: BMAL1-deficient VAT T_{regs} were preferentially lost during competitive transfers and in heterozygous $T_{reg}^{Bmal1\Delta}$ females. After 16 weeks of high-fat diet feeding, VAT inflammation was increased in mice harboring BMAL1-deficient T_{regs}, and the remaining cells lost the transcriptomic signature of bona fide VAT T_{regs}. Unexpectedly, VAT T_{regs} suppressed adipocyte lipolysis, and BMAL1 deficiency specifically in T_{regs} abrogated the characteristic diurnal variation in adipose tissue lipolysis, resulting in enhanced suppression of lipolysis throughout the day. These findings argue for the importance of the cell-intrinsic clock program in optimizing VAT T_{reg} function and fitness.

INTRODUCTION

Regulatory T cells (T_{regs}), particularly those expressing the transcription factor (TF) Foxp3, play an essential role in restraining overexuberant immune responses. Although early studies focused on T_{regs} circulating through lymphoid organs, it is by now well established that T_{regs} are located in nonlymphoid tissues as well. These so-called "tissue T_{regs}" have unique transcriptomes, T cell receptor (TCR) repertoires, and growth/survival factor dependencies that enable them to thrive in particular tissue environments, where they help maintain homeostasis (*1*). Although tissue T_{regs} exhibit a diversity of phenotypes and functions, they also share transcriptomic modules that set them apart from their lymphoid-organ counterparts (*1*, *2*). Pathways related to circadian rhythms are among the up-regulated pathways shared most prominently, raising the question of whether tissue T_{regs} are subject to distinct diurnal regulation.

Mammalian circadian rhythms evolved to anticipate and adapt to diurnal variations in the environment. A set of "core-clock" genes encodes the molecular drivers of this process, the expression, activity, and degradation of which form an autoregulatory feedback loop lasting approximately 24 hours (*3*). Heterodimeric complexes of BMAL1:CLOCK drive a core component of circadian transcription, including genes encoding its inhibitors, PER and CRY, and genes specifying its transcriptional regulators, the REV-ERBs and ROR [reviewed in (*3*)]. These molecular oscillators are stratified into a hierarchy of central and peripheral pacemakers according to whether they are localized in cells of the suprachiasmic nucleus of the brain or in cells of peripheral tissues. Peripheral clocks interpret synchronization signals from the central pacemaker, which is primarily synchronized by light, and from other environmental cues, like feeding and temperature, to generate cell-intrinsic rhythmicity (*4*–*6*).

Our understanding of circadian regulation of T cells and of the functions of their core-clock genes is just beginning to emerge. Rhythmic T cell migration between the circulation and lymphoid organs is the best-described circadian behavior: in mice, peak numbers of lymphocytes are found in circulation around zeitgeber time (ZT) 5 (ZT0 signaling onset of the light period) and in lymphoid organs around ZT13 (*7*–*10*). In addition, naïve murine T cells isolated during the day are more likely to differentiate into T helper 17 (T_H17) cells than those taken at night (*11*). However, core-clock genes were reported to be dispensable for T cell differentiation and for their responses to bacterial and viral infection (*12*), and expression of core-clock genes in splenic T_{regs} seemed to lack rhythmicity (*13*). Thus, the contexts wherein T_{regs} are subject to circadian regulation, as well as the consequences of such regulation, remain in question.

We decided to investigate the importance and function of circadian rhythms in the paradigmatic tissue-T_{reg} population found in epididymal visceral adipose tissue (VAT) of lean mice (*14*). Thymic T_{regs} seed VAT in the first weeks of life, where they proliferate indolently until they dominate the $CD4^+$ T cell pool around 20 to 30 weeks of age (*15*). Their accumulation and survival depend on a unique transcriptome largely driven by the critical transcriptional

[1]Department of Immunology, Harvard Medical School, Boston, MA, USA. [2]Institute for Diabetes, Obesity, and Metabolism, Perelman School of Medicine, University of Pennsylvania, Philadelphia, PA, USA. [3]Division of Endocrinology, Diabetes and Metabolism, Department of Medicine, Perelman School of Medicine, University of Pennsylvania, Philadelphia, PA, USA. [4]Department of Genetics, Perelman School of Medicine, University of Pennsylvania, Philadelphia, PA, USA. [5]Evergrande Center for Immunologic Diseases, Harvard Medical School and Brigham and Women's Hospital, Boston, MA, USA.
*Corresponding author. Email: cbdm@hms.harvard.edu

regulator of adipocyte differentiation, peroxisome proliferator–activated receptor–γ (PPARγ), as well as on their TCRs and cytokines such as interleukin-33 (IL-33) (*15*–*18*). VAT T_{regs} regulate local and systemic metabolic tenor by controlling both immunologic and nonimmunologic cells (*14*, *16*, *17*).

Combining population-level and single-cell transcriptomics, adoptive transfer experiments, genetic ablation, obesity-inducing challenges, lipolysis assays, and cytofluorimetry-based single-cell metabolic assays, we uncovered a role for the cell-intrinsic clock in promoting the fitness of VAT, but not splenic, T_{regs}, regulating, for example, adipose tissue lipolysis. The heightened circadian regulation in T_{regs} operating in non–lymphoid tissue environments re-emphasizes their adaptability and notable divergence from their lymphoid organ counterparts.

RESULTS

Elevated expression of core-clock genes in VAT T_{regs}

Because pathways related to circadian rhythms appeared to be up-regulated in tissue T_{regs} (*1*, *2*), we used published microarray data to compare expression of the core-clock genes in VAT (*16*), muscle (*19*), and colonic lamina propria (*20*) T_{regs} with that of their lymphoid organ counterparts. Core-clock genes, across all major arms of the cell-intrinsic clock machinery (Fig. 1A), were expressed at higher levels in T_{regs} from nonlymphoid than lymphoid tissues (Fig. 1B and fig. S1A). Focusing on VAT, we found much less evident up-regulation of the core-clock genes in conventional $CD4^+$ T cells (T_{convs}) than in T_{regs} (Fig. 1C and fig. S1B). Data from a T_{reg} adoptive transfer system confirmed that the VAT microenvironment up-regulated core-clock gene expression: Transfer of T_{regs} from a VAT-T_{reg} TCR-transgenic (tg) mouse line (*18*) into non-tg recipients resulted in accumulation of donor T_{regs} with elevated expression of core-clock genes in VAT in comparison with spleen (Fig. 1D and fig. S1C). Thus, expression of core-clock genes was elevated in tissue T_{regs}, VAT T_{regs} in particular, in comparison with their splenic counterparts, an increase induced by the tissular microenvironment.

Rhythmic expression of VAT-T_{reg} core-clock genes

We next assessed diurnal expression profiles of the core-clock genes by population-level RNA sequencing (RNA-seq) of cytofluorimetrically sorted VAT T_{regs}. Plotting gene expression versus time, where ZT0 denotes the onset of the light phase and ZT12 the dark phase, revealed that expression of most of the core-clock genes (such as *Bmal1*, *Per1–3*, and *Nr1d1,2*) exhibited significant rhythmicity in VAT T_{regs} (Fig. 2A). The times of peak core-clock gene expression in VAT T_{regs} were similar to those previously reported for liver cells (*21*, *22*), reinforcing the notion that peripheral tissues are usually synchronized. Expression of a few core-clock genes, specifically *Cry1–2* and *Rorα*, lacked rhythmicity in VAT T_{regs}, which is

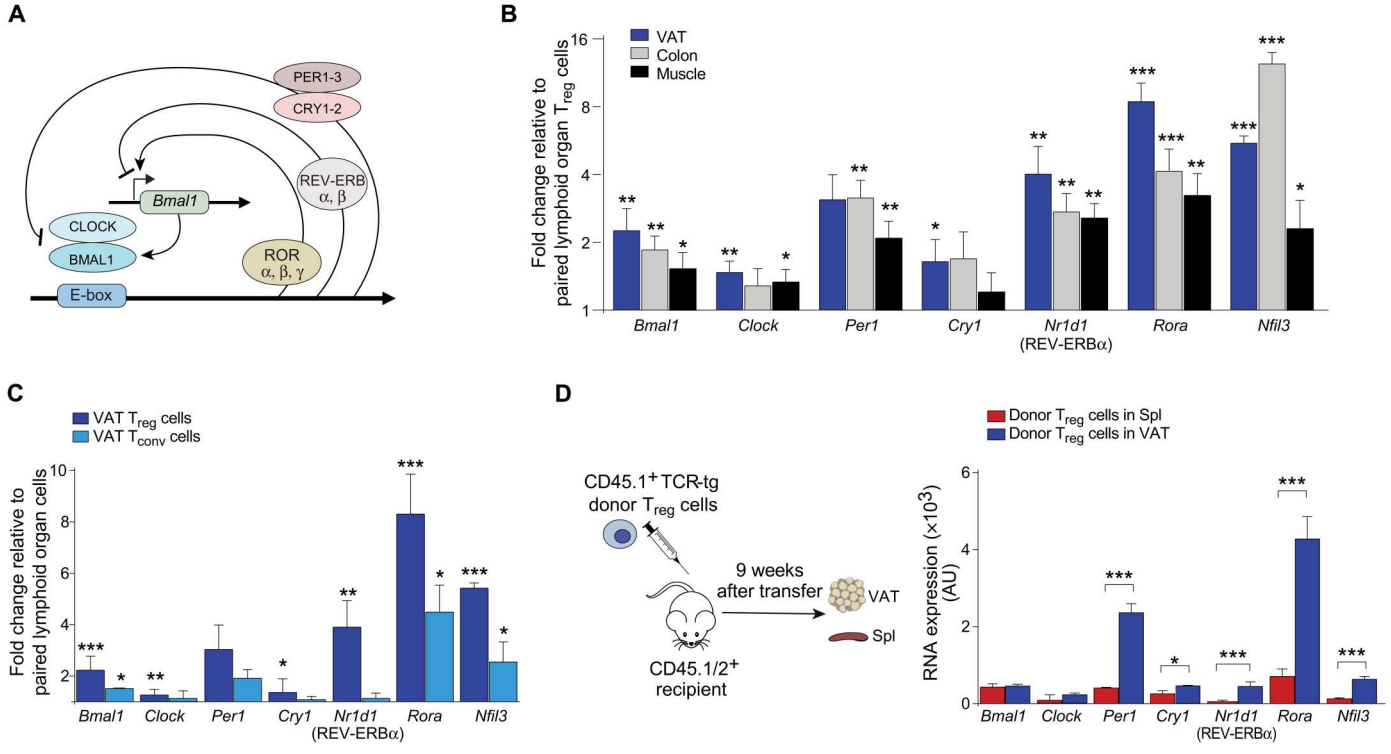

Fig. 1. Up-regulation of core-clock gene expression in VAT T_{regs}. (**A**) Schematic of the cell-intrinsic circadian rhythms executed by core-clock gene products. (**B**) Core-clock gene expression by tissue T_{regs} from published microarray data: VAT (*16*), skeletal muscle 4 days after cardiotoxin injury (*19*), and colonic lamina propria (*20*). T_{regs} in comparison with lymphoid organ T_{regs} from the same mice. (**C**) Core-clock gene expressions in VAT-T_{reg} or VAT-T_{conv} cells, from published microarray data on retired male breeders (*28*) in comparison with lymphoid organ T_{regs} or T_{convs} from the same mice. (B and C) $^*P \le 0.05$, $^{**}P \le 0.01$, and $^{***}P \le 0.001$ according to Student's *t* test comparing expression in tissue versus paired lymphoid organ T_{regs}. (**D**) Core-clock gene expression at ZT0 (onset of light phase) in donor T_{regs} 9 weeks after transfer in recipients' VAT and spleen. T_{regs} from *Foxp3-Cre.YFP*$^+$CD45.1$^+$TCR-tg$^+$ donors were transferred into *Foxp3-Cre.YFP*$^+$CD45.1/2$^+$ recipients. FDR: $^*\le 0.05$, $^{**}\le 0.01$, and $^{***}\le 0.001$ according to the quasi-likelihood *F* test by EdgeR. $n \ge 3$ per condition. Spl, spleen; AU, arbitrary units.

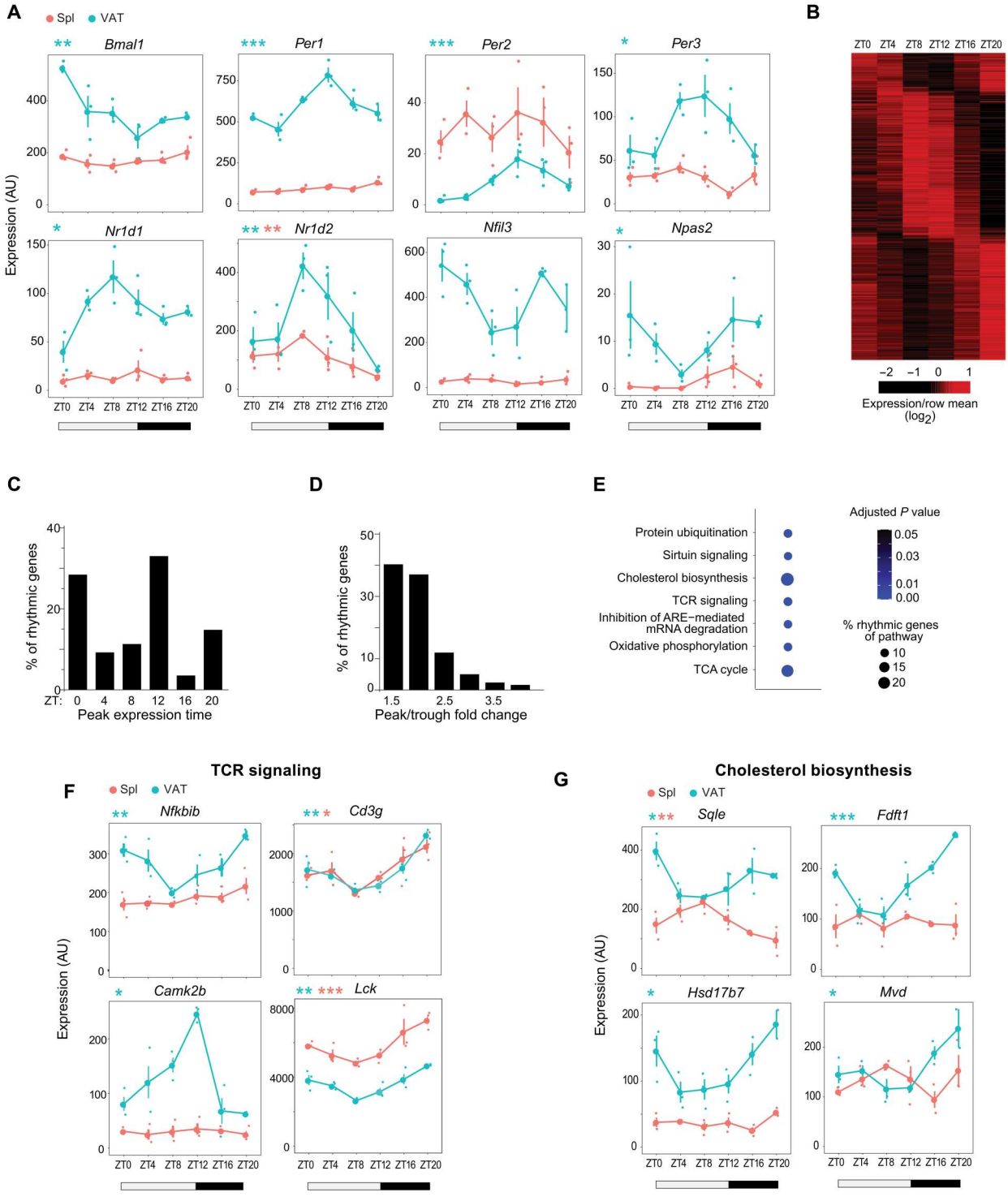

Fig. 2. Rhythmic expression of core-clock genes and other loci in VAT T_{regs}. Retired B6 male breeders (>35 weeks old) were euthanized every 4 hours during a 12-hour light/12-hour dark cycle. ZT0 signals onset of the light period (see bars below relevant panels). T_{regs} were sorted as $CD4^+CD25^+$. (**A**) Expression of core-clock genes over time. (**B**) Heatmap of rhythmically expressed genes in VAT T_{regs}. (**C**) Distribution of the time of peak expression for rhythmically expressed genes in VAT T_{regs}. (**D**) Fold change of maximum/minimum gene expression over time in rhythmically expressed genes. (**E**) Ingenuity pathway analysis of rhythmic genes. (**F** and **G**) Expression profiles of selected rhythmically expressed genes in the TCR signaling pathway (F) and cholesterol biosynthesis pathways (G) from (E). Circadian rhythmicity determined by JTK_Cycle. $^*P \leq 0.05$, $^{**}P \leq 0.01$, and $^{***}P \leq 0.001$. $n = 3$ for each time point from ZT0 to ZT16, $n = 2$ for ZT20. Flow cytometric gating strategies for all quantified or isolated cell types can be found in fig. S7.

expected given the report that not all core-clock genes are rhythmically expressed in peripheral tissues (*23*). In stark contrast, rhythmicity of core-clock genes in splenic T_{regs} appeared muted and was not statistically significant, with the exception of *Nr1d2* (Fig. 2A).

Looking beyond the core-clock genes to loci they might regulate, we identified over 600 genes with rhythmic expression in VAT T_{regs} after filtering out genes with low expression or a period of rhythmicity less than 16 hours (Fig. 2B and table S1). Peak expression of most of these genes was near either ZT0 or ZT12 (Fig. 2C), with about a 1.5- to 2-fold change in expression between their highest and lowest expression (Fig. 2D). Pathway analysis on the rhythmically expressed genes in VAT T_{regs} revealed an enrichment in pathways related to protein ubiquitination, sirtuin signaling, cholesterol biosynthesis, T cell activation, and mitochondrial metabolism (Fig. 2E). Transcripts encoding molecules involved in TCR signaling and cholesterol biosynthesis peaked mostly around ZT0/24 (Fig. 2, F and G). Thus, clock genes were rhythmically expressed in VAT T_{regs} but generally not in splenic T_{regs}.

Core-clock gene products enhance the fitness of VAT T_{regs}

To assess the functional importance of the T_{reg}-intrinsic clock, we abrogated expression of BMAL1 (which drives the forward loop of the clock and thereby promotes rhythmicity) specifically in T_{regs} by crossing *Foxp3-Cre.YFP* mice with a *Bmal1*$^{flox/flox}$ strain (*24*). The mutant offspring will hereafter be referred to as $T_{reg}^{Bmal1\Delta}$ mice (*Foxp3-Cre.YFP*$^{+}$*Bmal1*$^{flox/flox}$) as opposed to the $T_{reg}^{Bmal1WT}$ controls (*Foxp3-Cre.YFP*$^{+}$*Bmal1*$^{wt/wt}$). We confirmed that the mutant T_{regs} lacked the floxed exon 8 (fig. S2A) by inspecting pile-ups generated from population-level RNA-seq. Furthermore, we verified the specificity of deletion under the *Foxp3-Cre* driver by reverse transcription quantitative polymerase chain reaction (qPCR) and observed that *Bmal1* expression was substantially decreased in T_{regs} but remained unaffected in CD4^{+} T_{convs} or CD8^{+} T cells from the spleen (fig. S2B). As expected, loss of BMAL1 led to significant alterations in the expression of other core-clock genes at ZT0 in sorted VAT T_{regs}. Specifically, there was elevated expression of some genes, such as *Cry1* and *Npas2*, and reduced expression of others, such as *Nr1d1* and *Nr1d2* (Fig. 3A).

Because the VAT-T_{reg} compartment in adult mice receives little contribution from circulating T_{regs} (*15*), we expected diurnal variation in the circulation of lymphoid organ T cells (*8*) to have little impact on the VAT-T_{reg} pool size. Accordingly, the number and fraction of VAT T_{regs} remained similar at ZT0 and ZT12 and between $T_{reg}^{Bmal1WT}$ and $T_{reg}^{Bmal1\Delta}$ mice at ZT0 (Fig. 3B and fig. S2C). The frequency of T_{regs} in the spleen also lacked diurnal variation and appeared normal in the absence of BMAL1 (fig. S2D).

We suspected that the T_{reg}-intrinsic clock might promote fitness without affecting accumulation at homeostasis. Thus, we assessed the fitness of BMAL1-deficient T_{regs} in a competitive adoptive transfer system. When polyclonal lymphoid organ T_{regs} are transferred under this protocol, they do not accrue in VAT; however, T_{regs} from the VAT-T_{reg} TCR-tg mouse line mentioned above do accumulate after transfer, reflecting efficient recognition of their TCR's ligand (*18*). We generated *Foxp3-Cre.YFP*$^{+}$.CD45.1^{+}.TCR-tg^{+}*Bmal1* wild type (WT) and *Foxp3-Cre.YFP*$^{+}$.CD45.2^{+}.TCR-tg^{+}*Bmal1* Δ donor strains. *Bmal1* WT and *Bmal1* Δ T_{regs} were transferred at a 1:1 ratio into *Foxp3-Cre.YFP*$^{+}$.CD45.1/2^{+} recipients, and donor-T_{reg} accumulation was quantified in the VAT and spleen at various time points thereafter (Fig. 3C). Donor T_{regs} were first detected in VAT 6 weeks after transfer, when the *Bmal1* WT and *Bmal1* Δ cells were present at an equal ratio. By 7.5 to 9 weeks, the *Bmal1* Δ population had undergone a preferential expansion, representing over 70% of the total donor-T_{reg} pool. However, this transient dominance was followed by a crash of the *Bmal1* Δ T_{reg} population, such that mutant cells represented less than 10% of donor T_{regs} 12 weeks after transfer (Fig. 3, D and E). Similar dynamics were observed for donor-T_{reg} numbers (fig. S2E). In contrast, *Bmal1* WT and *Bmal1* Δ T_{regs} persisted equally well in the spleen at 12 weeks after transfer (Fig. 3F), suggesting a tissue-specific role for the T_{reg}-intrinsic clock in promoting fitness. The reduced number of *Bmal1* Δ cells was not due to a lack of proliferation because the fractions of Ki67^{+} donor cells were similar in the presence and absence of *Bmal1* (Fig. 3G), nor did it appear to reflect migration to other tissues (fig. S2F). We also verified that the reduction of *Bmal1* Δ T_{regs} was not due to the CD45 allele they expressed; competitive transfer of CD45.1^{+} and CD45.2^{+} WT cells led to similar persistence in the recipients' VAT (fig. S2G). Therefore, loss of *Bmal1* Δ donor cells was most likely issued from a difference in survival.

Last, loss of fitness was not restricted to adoptive transfer settings or to TCR-tg T_{regs}. Because the *Foxp3* gene maps to the X chromosome, random X-inactivation in female mice randomly silences one of the *Foxp3* alleles in each cell. Thus, in *Foxp3-Cre.YFP*$^{+/-}$*Bmal1*$^{flox/flox}$ heterozygotes, half of the T_{regs} express BMAL1 (Cre^{-}) while half do not (Cre^{+}). The number and fraction of Cre^{+} T_{regs} in the gonadal fat of female heterozygotes were substantially lower than those of coresident Cre^{-} T_{regs} (Fig. 3H). Only 20% of total T_{regs} were Cre^{+}, and their numbers were significantly less than Cre^{-} T_{regs} (Fig. 3H). As expected, control *Foxp3-Cre.YFP*$^{+/-}$ females without *Bmal1* deletion did not show these differences: Cre^{+} cells represented 40% of total T_{regs} in the gonadal fat, and the numbers of Cre^{+} and Cre^{-} T_{regs} were similar (fig. S2, H and I).

To rule out transcriptional effects of *Bmal1* unrelated to its role in circadian rhythms, we performed analogous experiments on another core-clock gene, *Nr1d1*, encoding REV-ERBα. Like the $T_{reg}^{Bmal1\Delta}$ strain, *Foxp3-Cre.YFP*$^{+}$.*Nr1d1*$^{flox/flox}$ (hereafter referred to as $T_{reg}^{Nr1d1\Delta}$) mice showed normal accumulation of VAT T_{regs} (fig. S2J). However, donor *Nr1d1* Δ T_{regs} did not persist like *Nr1d1* WT T_{regs} did in the recipients' VAT 12 weeks after transfer (Fig. 3, I and J), whereas competitively transferred T_{regs} of the two genotypes were maintained equally well in the spleen (Fig. 3K). Because *Nr1d1* Δ T_{regs} showed no reduction in *Bmal1* expression at ZT12 (fig. S2K), consistent with the role of REV-ERBα in repression of *Bmal1* expression, the loss of competitive fitness of both *Bmal1* Δ and *Nr1d1* Δ donor cells indicated that circadian rhythms, rather than expression of *Bmal1* per se, promoted VAT-T_{reg} fitness.

Diurnal variation of the activation state of ST2^{+} T_{reg} subtypes

As a preliminary step in understanding the mechanisms underlying diurnal control of VAT-T_{reg} fitness, we performed single-cell (sc)RNA-seq on VAT T_{regs} at ZT0 and ZT12 from $T_{reg}^{Bmal1WT}$ and $T_{reg}^{Bmal1\Delta}$ animals. To permit simultaneous isolation of cell populations at ZT0 and ZT12, we housed half of the experimental animals in a room with the opposite light cycle for at least 14 days (*25*) and verified that the animals therein indeed entrained to the

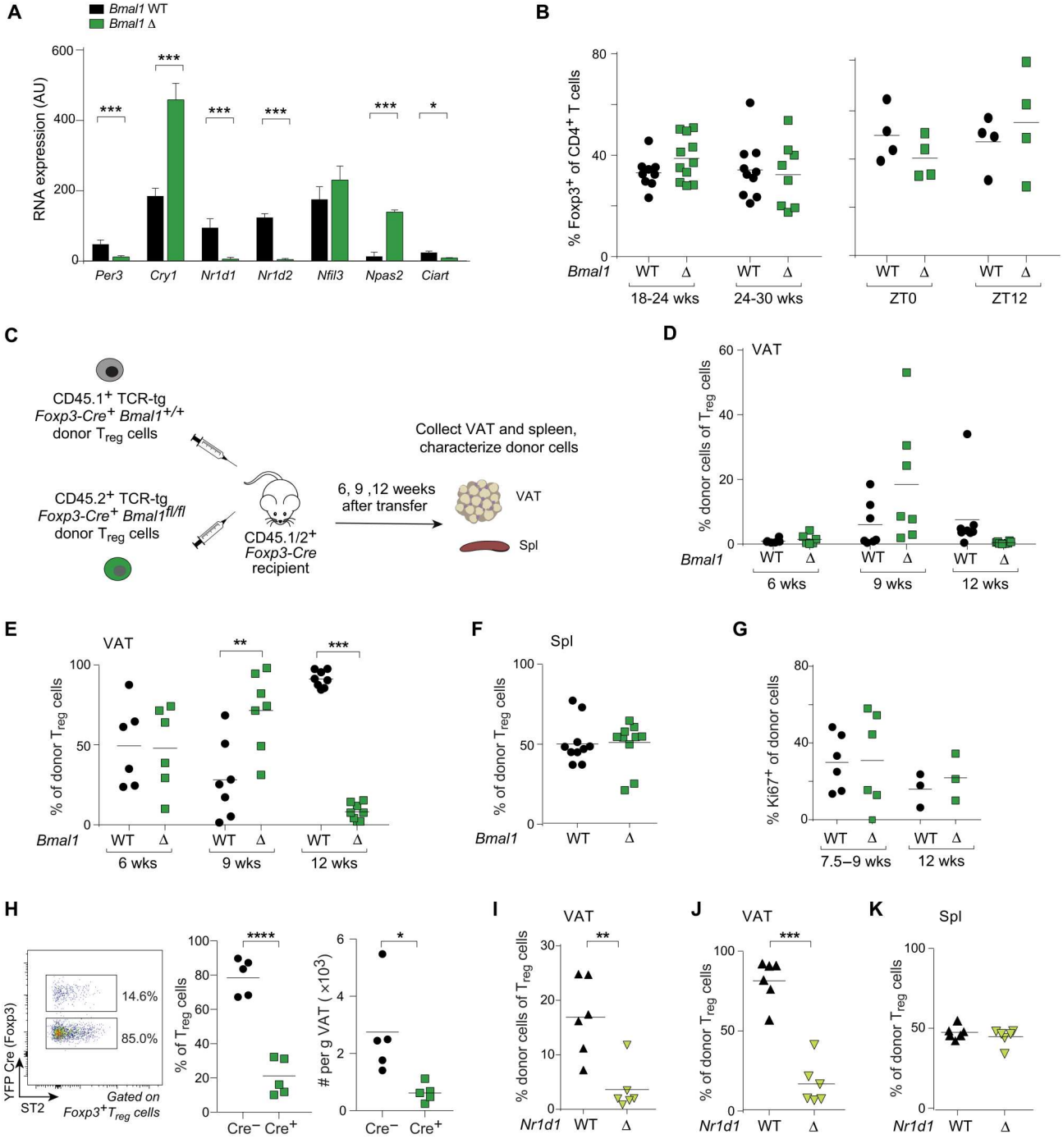

Fig. 3. Loss of competitive fitness in VAT T_{regs} in the absence of BMAL1 or REV-ERBα. (**A** and **B**) VAT T_{regs} were isolated at ZT0 from 18- to 30-week-old male $T_{reg}^{Bmal1WT}$ (WT) or $T_{reg}^{Bmal1\Delta}$ (Δ) mice. (A) Expression of core-clock genes at 18 weeks of age determined by RNA-seq analysis. (B) Fraction of VAT T_{regs} across age groups at ZT0 (left) and at ZT0 versus ZT12 (right). Left: Pooled data from four independent experiments; right: representative data of three independent experiments. $n \geq 2$ per group per experiment. (**C** to **G**) Competitive transfer of a 1:1 mix of T_{regs} from 6- to 8-week-old male mice of the indicated genotype into 8- to 10-week-old recipients, as schematized in (C). (D and E) Fractions of *Bmal1* WT and *Bmal1* Δ donor cells expressed as a percentage of total T_{regs} (D) or of total donor T_{regs} (E) in the recipients' VAT. (F) Similar to (E) but from the recipients' spleens 12 weeks after transfer. (G) Fraction of donor cells in cycle (Ki67+). For 9 and 12 weeks after transfer, representative data of at least three experiments, $n \geq 3$ per experiment. (**H**) T_{regs} in gonadal fat of *Foxp3-Cre*$^{+/-}$.*YFP*$^{+/-}$*Bmal1*$^{flox/flox}$ female heterozygotes. Fraction of Cre$^-$ versus Cre$^+$ T_{regs}; left: representative flow plot; middle: frequency; right: cell number. (**I** to **K**) Competitive transfer of a 1:1 mix of T_{regs} from the indicated genotypes into *Foxp3-Cre.YFP*$^+$CD45.1/2$^+$ recipients and assessed 12 weeks after transfer. Data pooled from two independent experiments. (I and J) Fractions of *Nr1d1* WT and *Nr1d1* Δ donors expressed as a percentage of total T_{regs} (I) or of total donor T_{regs} (J) in the recipient's VAT. (K) Same as (I), but from the recipients' spleens. *$P \leq 0.05$, **$P \leq 0.01$, and ***$P \leq 0.001$ according to Student's *t* test for the transfer experiments; quasi-likelihood *F* test by EdgeR for RNA-seq data. wks, weeks. Flow cytometric gating strategies for all quantified or isolated cell types can be found in fig. S7.

new light regimen (fig. S3A). Cells from the four conditions were separately hashtagged and encapsulated together. After demultiplexing, we obtained robust scRNA-seq data for over 6500 VAT $CD4^+$ T cells, with an average of 1300 genes detected per cell.

Overlay of *Foxp3* expression on a Uniform Manifold Approximation and Projection (UMAP) of the pooled datasets allowed us to distill the T_{reg} compartment (fig. S3B) consisting of over 2000 cells. We then reclustered the T_{regs}, revealing five distinct subtypes (Fig. 4A). The p1 $ST2^+$, p2 $ST2^+$, $Tbet^+$, $IL18R^+$, and resting clusters were distinguished by divergent and diagnostic gene expression profiles (Fig. 4B). For instance, the resting cluster expressed elevated levels of *Sell* and *Ccr7*; the $Tbet^+$ cluster expressed higher levels of *Cxcr3* and *Tbx21*; and the $IL18R^+$ cluster expressed elevated levels of *Il18r*, *Cxcr3*, and *S1pr1*. Two clusters expressed *Il1rl1*, encoding ST2: p1 with higher levels of *Areg*, *Nfkbia*, and *Junb* transcripts and p2 with elevated *Ly6c* expression (Fig. 4B). A differential density map revealed enrichment of the p1 over the p2 $ST2^+$ subtype in ZT0 VAT T_{regs} and increased representation of the $Il18r^+$ subtype (Fig. 4C).

To validate these findings at the protein level, we searched for differentially expressed genes whose products could be detected by flow cytometry. Antibodies recognizing CD62L, ST2, IL18R, CD39, CD69, and CD25 distinguished the five T_{reg} clusters defined in Fig. 4A (fig. S3C). For the p1 and p2 $ST2^+$ clusters, levels of *Cd69*, *Cd44*, and *Il2ra* transcripts were all higher in the p1 cluster, whereas *Ly6c* transcript levels were augmented in the p2 cluster (Fig. 4D). However, by flow cytometry, cell-surface expression of only CD69 distinguished the two subtypes of $ST2^+$ cells. $CD69^{high}$ $ST2^+$ T_{regs} showed a higher mean fluorescence intensity (MFI) of CD44 and CD25 staining and a lower MFI of Ly6c staining compared with those of $CD69^{low}$ $ST2^+$ T_{regs}, mirroring the scRNA-seq data (fig. S3D). Consistent with the enrichment of p1 $ST2^+$ T_{regs} at ZT0 (Fig. 4C), the fraction of $CD69^{high}$ cells was significantly higher within the $ST2^+$ T_{reg} population at ZT0 compared with ZT12 (Fig. 4E). In contrast, splenic T_{regs} showed a constant component of $CD69^{high}$ cells (Fig. 4F).

We then used the scRNA-seq data to explore differences between the p1 and p2 $ST2^+$ subtypes and to examine their interrelationships. Consistent with the higher CD44, CD25, and CD69 expressions, which are canonical T cell activation markers, T_{regs} of the p1 $ST2^+$ subtype appeared to be more activated. Pathway analysis identified heightened nuclear factor κB (NF-κB) and TCR signaling pathways (Fig. 4G), and transcripts encoding activation markers such as IκBα, NR4A1, EGR1, and JUNB were expressed at an elevated level (Fig. 4H). Furthermore, p1 $ST2^+$ cells expressed higher levels of transcripts encoding T_{reg} effector molecules such as *Areg*, *Ctla4*, and *Il10* (Fig. 4I) as well as transcripts encoding prosurvival molecules such as *Tnfaip3*, *Bcl2a1b*, and *Il10ra* (Fig. 4J). On the other hand, a higher fraction of p2 $ST2^+$ cells were $Ki67^+$, indicative of more cells in cycle (fig. S3E); thus, the two subtypes might reflect a balance of activation versus proliferation. RNA velocity analysis, which predicts the likely future state of a cell on the basis of the ratio of spliced to unspliced transcripts (*26*, *27*), revealed distinct trajectories at the two time points. At ZT12, a trajectory from the p2 toward the p1 $ST2^+$ subtype was predicted. That trajectory was absent at ZT0; instead, a subset of p1 $ST2^+$ cells exhibited a trajectory toward the p2 subtype (fig. S3F). In brief, then, the VAT-T_{reg} compartment includes multiple T_{reg} subtypes. Diurnal variation was seen in the relative contributions of the p1 and p2 subtypes of $ST2^+$ cells.

Heightened activation state of *Bmal1* Δ VAT T_{regs}

Diurnal variations within the $ST2^+$ T_{reg} population raised the question of whether they depended on the T_{reg}-intrinsic circadian clock. Analysis of cell density differences on the UMAP reproduced from Fig. 4A (Fig. 5A, left) revealed an enrichment in $ST2^+$ T_{regs}, particularly the p1 $ST2^+$ subtype, at both ZT0 (Fig. 5A, center) and ZT12 (Fig. 5A, right) in *Bmal1* Δ compared with *Bmal1* WT T_{regs}. Furthermore, *Bmal1* Δ T_{regs} showed an enrichment of the p1 $ST2^+$ subtype at both ZT0 and ZT12 (Fig. 5A), in contrast to WT cells, for which we observed a diurnal switch in the dominant $ST2^+$ subtype (Fig. 4C), suggesting that *Bmal1* Δ VAT T_{regs} might be constitutively activated. Population-level RNA-seq revealed heightened activation terms such as "T_H1 and T_H2 activation", "tumor necrosis factor receptor 2 (TNFR2) signaling," and "IL-2 signaling" as well as elevated expression of genes encoding cytokine common γ-chain receptors (*Il2ra* and *Il7r*) and members of the NF-κB signaling pathway (*Nfkbia*, *Nfkb1*, and *Traf1*) in *Bmal1* Δ cells (Fig. 5B and fig. S4A). Consistent with the scRNA-seq data, $T_{reg}^{Bmal1\Delta}$ mice had elevated fractions of $ST2^+$ T_{regs} (Fig. 5C), which translated into an enrichment of the canonical VAT-T_{reg} signature (Fig. 5D) (*28*). Transcripts up-regulated in the p1 versus p2 $ST2^+$ clusters were also enriched in the *Bmal1* Δ T_{reg} transcriptome (Fig. 5E). According to flow cytometric analysis, the fraction of $CD69^{high}$ cells within the $ST2^+$ VAT-T_{reg} population was higher in $T_{reg}^{Bmal1\Delta}$ than in $T_{reg}^{Bmal1WT}$ mice (Fig. 5F), consistent with an enrichment of the p1 $ST2^+$ subtype. This enrichment was accompanied by a nonsignificant relative decrease in the $Tbet^+$ ($Il18r^-$) subtype in *Bmal1* Δ VAT T_{regs} (fig. S4B). In contrast, the fraction of $CD69^{high}$ T_{regs} was the same in $T_{reg}^{Bmal1WT}$ and $T_{reg}^{Bmal1\Delta}$ spleens (Fig. 5F). Consistent with the transcriptomic data, the MFI of CD44 staining was significantly higher, and the MFI of CD25 staining trended higher in *Bmal1* Δ than in *Bmal1* WT VAT T_{regs} (Fig. 5G). These variations were not present in splenic T_{regs} (fig. S4C).

Male and female mice have distinct gonadal VAT T_{reg} compartments (*18*, *29*, *30*). We identified five T_{reg} subtypes in T_{regs} isolated from the gonadal fat (gVAT) of 8- to 12-week-old female mice using the gating strategy adopted from our single-cell analysis (fig. S4D). The fraction of $ST2^+$ cells was lower in female than in male mice, consistent with prior reports (*29*, *30*). Similar to males, female *Bmal1* Δ mice exhibited an increased fraction of gVAT $ST2^+$ T_{regs} and a decrease in the $Tbet^+$ ($IL18r^-$) T_{reg} subtype (fig. S4E). However, representation of the $CD69^{hi}$ p1 subtype within the $ST2^+$ population was unchanged in mutant T_{regs} (fig. S4E).

A heightened activation state in the absence of *Bmal1* likely also explained the preferential expansion of the *Bmal1* Δ donor–derived T_{reg} population at 9 weeks after competitive transfer. Population-level RNA-seq on sorted *Bmal1* WT and mutant donor-derived cells at this time point revealed an enrichment in activation pathways such as "TNF-α signaling via NF-kb" and "IL-2/Stat5 signaling" (fig. S4F). Expression of *Egr1*, *Nfkb1*, *Cd44*, *Il2ra*, and *Il7r* was increased in *Bmal1* Δ donor–derived cells (fig. S4G), because they were in the noncompetitive setting (fig. S4A). Flow cytometric analysis confirmed the expected increase in CD44 MFI in *Bmal1* Δ donor–derived cells 12 weeks after transfer (fig. S4H). Thus, *Bmal1* Δ T_{regs} showed an enrichment of the $ST2^+$ subtype in both

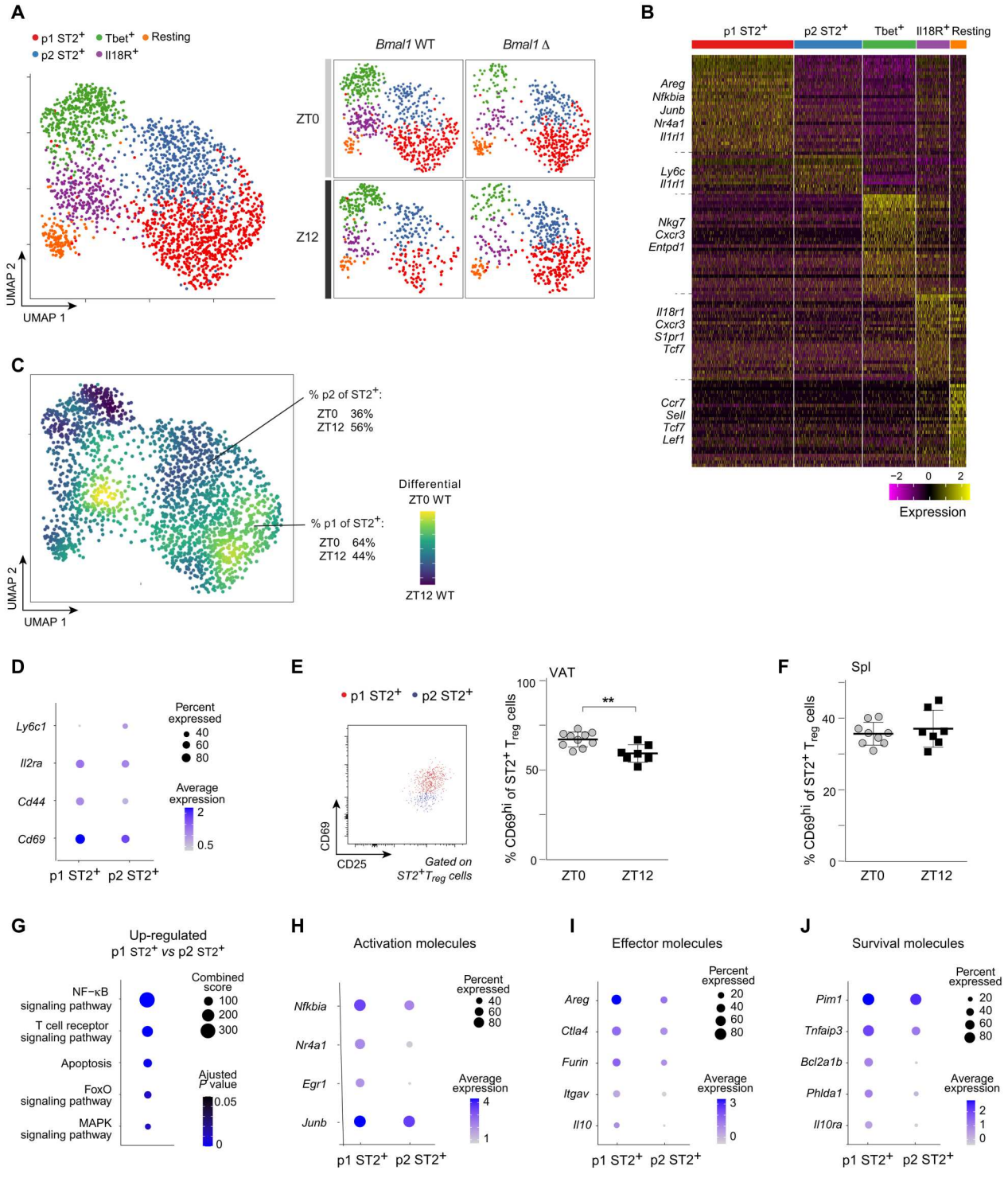

Fig. 4. Diurnal variation of activation state within the ST2$^+$ T$_{reg}$ population. (**A** to **D** and **G** to **J**) scRNA-seq analysis of 21- to 23-week-old *Foxp3-Cre.YFP*$^+$ (WT) and *Foxp3-Cre.YFP*$^+$*Bmal1*$^{flox/flox}$ (Δ) VAT T$_{regs}$ at ZT0 and ZT12. (A) Heterogeneity of VAT T$_{regs}$ visualized by UMAP. Left: a composite of all four conditions; right: disentangled plots for each condition. (B) Heatmap of top 30 differentially expressed genes of the clusters distinguished in (A). (C) Cell density differential between the UMAPs of ZT0 and ZT12 *Bmal1* WT VAT T$_{regs}$; frequencies of p1 and p2 subtypes of ST2$^+$ cells are indicated. (D) Differential RNA expression of cell-surface markers for flow cytometric distinction of p1 ST2$^+$ and p2 ST2$^+$ T$_{regs}$. (**E**) Fraction of CD69^{hi} VAT T$_{regs}$ at ZT0 or ZT12 in B6 mice. Left: Flow cytometric dot plot; right: summary data. (**F**) Fraction of CD69^{hi} splenic T$_{regs}$ at ZT0 and ZT12. (E and F) Pooled data from two independent experiments. (G) Kyoto Encyclopedia of Genes and Genomes pathway analysis by EnrichR of differentially expressed genes in cells of the p1 and p2 ST2$^+$ clusters. (H to J) Examples of differentially expressed genes encoding activation (H), effector (I), and survival (J) molecules. $^{**}P \leq 0.01$ by Student's *t* test. $n \geq 3$ per group per experiment. Flow cytometric gating strategies for all quantified or isolated cell types can be found in fig. S7.

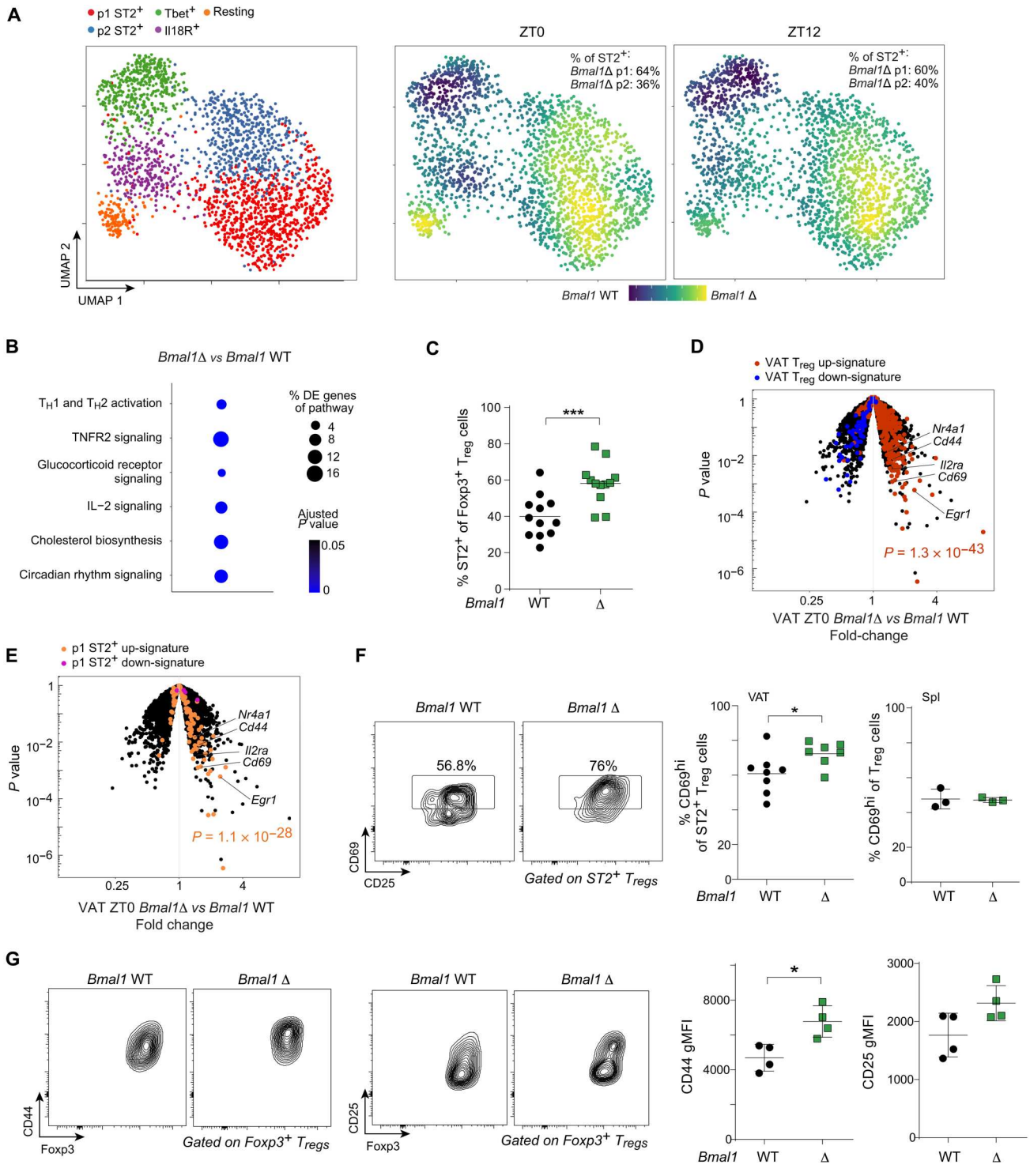

Fig. 5. Elevated activation state of *Bmal1* Δ T_{regs}. (**A**) Cell density differential comparing *Bmal1* WT and *Bmal1* Δ VAT T_{regs} at ZT0 (middle) and ZT12 (right). The left panel re-presents Fig. 4A for convenient and accurate comparison. (**B** to **D**) Population-level RNA-seq of *Bmal1* WT and *Bmal1* Δ VAT T_{regs} from 18-week-old male mice at ZT0. (B) Ingenuity pathway analysis. (C) Fraction of ST2$^+$ VAT T_{regs} from 18- to 30-week-old male mice at ZT0. (D) Volcano plot overlaid with up-regulated (red) and down-regulated (blue) VAT-T_{reg} signature genes (*28*). (**E**) Volcano plot overlaid with genes up-regulated in the p1 ST2$^+$ cluster (orange) or p2 ST2$^+$ cluster (pink). (**F**) Left: flow plot. Right: summary data showing fraction of CD69^{high} T_{regs} in VAT and spleen at ZT0 or ZT12. (**G**) Geometric MFI (gMFI) of CD44 (left and middle) and CD25 (right) expression at ZT0. For flow cytometric data, *$P \leq 0.05$, and ***$P \leq 0.001$ according to Student's *t* test. Flow cytometric gating strategies for all quantified or isolated cell types can be found in fig. S7.

male and female mice at steady state and were more activated than their WT counterparts in male mice and after adoptive transfer.

VAT T_{regs} enforce diurnal lipolysis

We next sought to identify the physiological function(s) of the cell-intrinsic clock in VAT T_{regs}. When fed on lean chow, $T_{reg}^{Bmal1\Delta}$ mice exhibited a small increase in adiposity compared with their WT littermates (Fig. 6A), without significant changes in their glucose tolerance or insulin sensitivity (fig. S5A). Because increased adiposity can result from reduced lipolysis, and given that the extent of adipose tissue lipolysis is known to oscillate diurnally (*31*), we interrogated the role of T_{regs} in this process. Systemic depletion of T_{regs}, achieved through diphteria toxin (DT) administration to >16-week-old Foxp3-DTR$^+$ mice (Fig. 6B), provoked a rapid decrease in epididymal VAT (eVAT) weight 3 days after DT injection (Fig. 6C), and the epididymal fat pads were visibly smaller (Fig. 6D), suggestive of increased lipolysis. To assess the lipolytic rate of adipose tissue, we explanted eVAT and stimulated it with norepinephrine (NE) in vitro as described previously (*32*, *33*). This approach circumvents the challenge of interpreting serum glycerol levels, which depend on both lipolytic output and peripheral organ uptake (*34*). Explants from T_{reg}-depleted animals were less sensitive to NE stimulation and resisted further lipolysis, expressed as micromolar release of glycerol per milligram VAT per hour, whereas basal glycerol release was similar (Fig. 6E). This diminished lipolysis in vitro likely resulted from an elevated lipolysis in vivo. For instance,

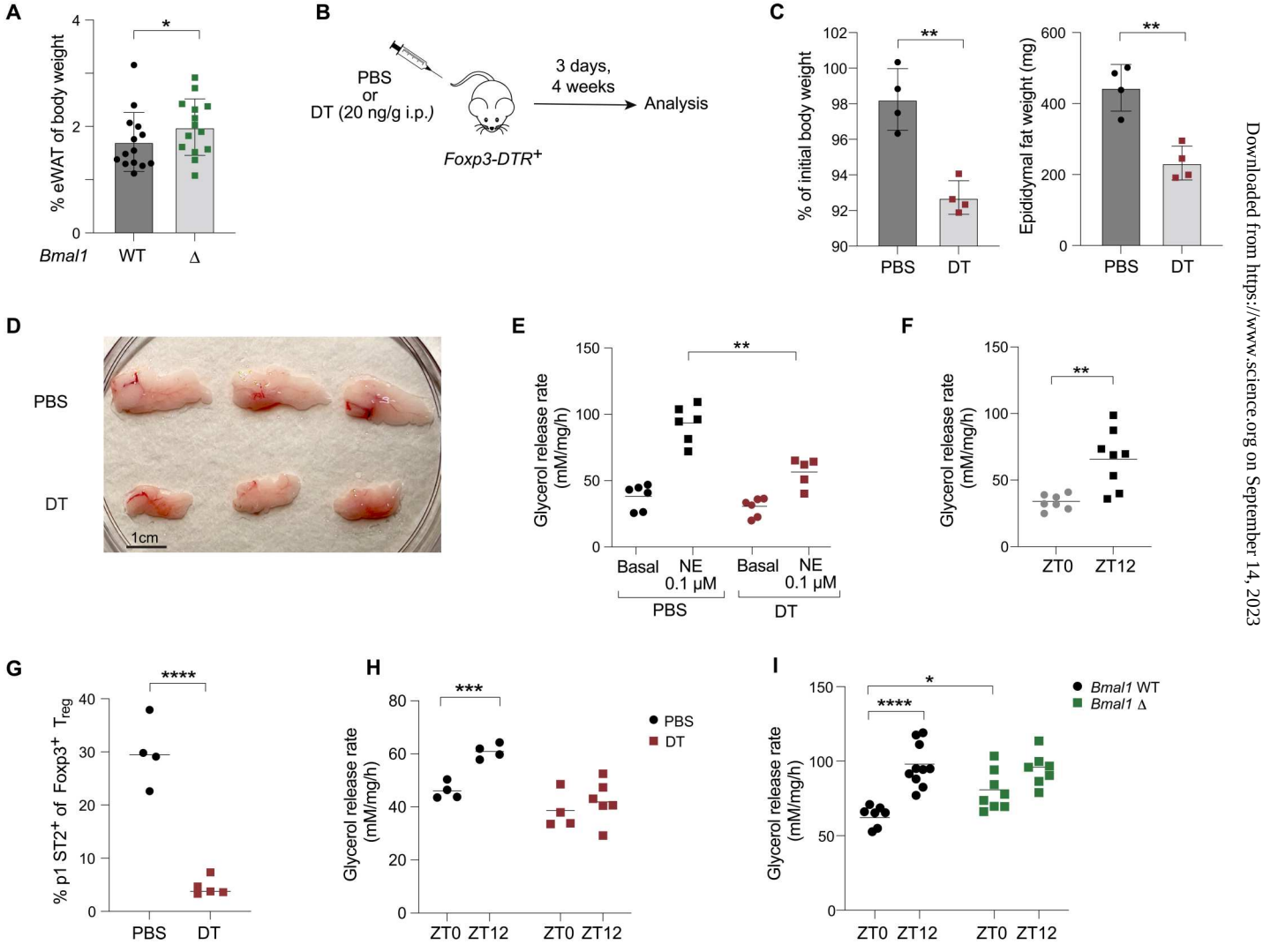

Fig. 6. VAT T_{regs} enforce diurnal lipolysis. (**A**) Body composition of 18- to 24-week-old male littermates. (**B** to **E** and **G** to **H**) Lipolysis experiments in 22- to 32-week-old male *Foxp3-DTR*$^+$ mice. (B) Schematic of DT injection and subsequent analyses. (C to E) Body and eVAT weight (C); photo of epididymal fat pad (D); in vitro glycerol release rate of VAT explants 3 days after DT injection at ZT12 (E); (**F**) in vitro glycerol release rate of VAT explants isolated from $T_{reg}^{Bmal1WT}$ male mice stimulated with 0.1 μM NE. (G to H) Fraction of p1 ST2$^+$ (CD69^{hi}) T_{regs} (G); in vitro glycerol release rate of VAT explants 4 weeks after DT injection stimulated with 0.1 μM NE (H). (**I**) In vitro glycerol release rate of VAT explants of 12- to 23-week-old $T_{reg}^{Bmal1WT}$ and $T_{reg}^{Bmal1\Delta}$ male mice stimulated with 0.1 μM NE pooled from two independent experiments. For in vitro lipolysis assays, each dot is one explant, and two explants were taken per mouse per condition. Paired Student's *t* test between littermate pairs was performed for (A). For other panels, *$P \leq 0.05$, **$P \leq 0.01$, ***$P \leq 0.001$, and ****$P \leq 0.0001$ according to Student's *t* test. DTR, diphteria toxin receptor; h, hour. Flow cytometric gating strategies for all quantified or isolated cell types can be found in fig. S7.

injection of the β3-adrenergic agonist CL316,243 (CL), which is well known to induce extensive lipolysis in vivo, into B6 mice also resulted in diminished lipolysis in vitro (fig. S5B).

eVAT explants taken at ZT12 underwent significantly more in vitro lipolysis in response to NE stimulation than did those taken at ZT0 (Fig. 6F), indicative of a diurnal rhythm in lipolysis. However, explants from mice deficient in the ST2$^+$ T_{reg} population, in particular the p1 subtype, did not exhibit this rhythmicity. Four weeks after DT injection, eVAT weight and VAT T_{reg} numbers had normalized in DT-injected mice (fig. S5C), but the fraction of p1 ST2$^+$ T_{regs} remained low (Fig. 6G). Explants from these animals exhibited constitutively low lipolysis in vitro (Fig. 6H), suggesting that p1 ST2$^+$ T_{regs} desensitized adipocytes to NE-induced lipolysis in vivo and were required for diurnal rhythmicity. Last, we assessed whether adipose tissue lipolysis was controlled by BMAL1 in T_{regs}. Diurnal rhythms of lipolysis in eVAT from $T_{reg}^{Bmal1\Delta}$ mice appeared blunted: In vitro lipolysis was elevated at both ZT0 and ZT12 after NE stimulation (Fig. 6I), indicative of reduced lipolysis in vivo and consistent with the increased adiposity of $T_{reg}^{Bmal1\Delta}$ mice (Fig. 6A). Thus, BMAL1 expression enables VAT T_{regs} to help enforce a diurnal rhythm in adipocyte lipolysis.

Accelerated activation but loss of fitness during high-fat diet challenge

The heightened activation state of *Bmal1* Δ T_{regs} in lean mice prompted us to characterize these mutant cells in the context of chronic activation such as high-fat diet (HFD)–induced obesity. Upon HFD feeding, the VAT-T_{reg} compartment responds in two distinct stages (*35*). VAT T_{regs} initially undergo a period of proliferation to counter mounting levels of inflammation (*35*), and their transcriptome shows an enrichment of the VAT-T_{reg} signature (*28*). With chronic HFD feeding, bona fide (ST2$^+$, KLRG1$^+$, and GATA3$^+$) VAT T_{regs} are greatly reduced, and the remnant cells lack the canonical VAT-T_{reg} signature (*14*, *28*, *35*). We fed $T_{reg}^{Bmal1WT}$ and $T_{reg}^{Bmal1\Delta}$ mice on a lean diet for 14 weeks to establish a normal pool of VAT T_{regs}, followed by HFD feeding for 4, 8, or 16 weeks (Fig. 7A). Weight gain was similar between the two genotypes (fig. S6A), as was the fraction and number of VAT T_{regs} (Fig. 7B and fig. S6B). However, after 4 weeks of HFD, transcriptional profiling of VAT T_{regs} revealed an enrichment of the VAT-T_{reg} signature in the mutants' T_{reg} transcriptome (Fig. 7C), associated with an elevated fraction of ST2$^+$ T_{regs} (fig. S6C) and higher cell-surface expression of CD44 and CD25 (Fig. 7D). In contrast, after 16 weeks of HFD, the VAT-T_{reg} signature was decreased in *Bmal1* Δ compared with *Bmal1* WT T_{regs} (Fig. 7E), suggestive of poor adaptation of *Bmal1* Δ T_{regs}. As a result, $T_{reg}^{Bmal1\Delta}$ mice had a higher fraction of CD11c$^+$ inflammatory macrophages (Fig. 7F) and a trend toward a greater accumulation of CD8$^+$ T cells at this time point (fig. S6D), indicative of increased VAT inflammation. In line with this notion, inflammatory pathways distinguished the eVAT depots from $T_{reg}^{Bmal1WT}$ and $T_{reg}^{Bmal1\Delta}$ mice after 16 weeks of HFD, as assessed by whole-tissue RNA-seq. Pathways related to interferon, IL-6, and TNF-α signaling were up-regulated in the VAT of $T_{reg}^{Bmal1\Delta}$ mice, whereas metabolic pathways such as fatty acid metabolism and oxidative phosphorylation were down-regulated (Fig. 7, G and H). Glucose and insulin tolerance, assessed at 7 and 9 weeks after HFD feeding, were similar between the two genotypes (fig. S6E). Thus, disruption of the cell-intrinsic clock impaired VAT T_{regs}' ability to adapt to the dysregulated VAT environment induced by HFD feeding.

Diurnal variation in mitochondrial electron transport chain activity

To explore potential mechanisms of how BMAL1 promoted T_{reg} fitness, we returned to the rhythmic pathways identified in VAT T_{regs} (Fig. 2E). Besides loci associated with TCR activation, we noted that the rhythmically expressed genes in VAT T_{regs} encoded molecules related to several mitochondrial oxidative metabolism pathways (Fig. 2E). Genes encoding components of the electron transport chain (ETC) and the tricarboxylic acid (TCA) cycle peaked between ZT20 and ZT0/24 according to JTK_CYCLE analysis (Fig. 8A). We analyzed the metabolic states of VAT T_{regs} at ZT0 and ZT12 to be consistent with other experiments, although analysis at ZT20 might have revealed even greater differences. Because of the very low number of VAT T_{regs} in individual mice, we could not implement conventional methods such as Seahorse assays to evaluate mitochondrial metabolism. Instead, we turned to flow cytometry to assess mitochondrial oxidative metabolism by measuring the mitochondrial membrane potential ($\Delta\Psi_m$) at steady state and after inhibition of adenosine 5′-triphosphate (ATP) synthase (complex V). Catabolism of molecules such as glucose, fatty acids, and amino acids ultimately feeds into the TCA cycle, where acetyl–coenzyme A is sequentially oxidized and electrons are passed to the ETC via reduction and oxidation of nicotinamide adenine dinucleotide (NAD^+)/reduced form of NAD^+ (NADH). Electron transport is coupled to translocation of protons from the mitochondrial matrix into the intermembrane space. Such proton translocation generates an electrochemical gradient across the inner mitochondrial membrane, the $\Delta\Psi_m$, which is primarily used to power ATP synthesis at complex V. Whereas the basal $\Delta\Psi_m$ is a function of proton influx and efflux, inhibition of complex V by oligomycin impairs proton influx to the matrix, and the resulting elevation of $\Delta\Psi_m$ is indicative of the extent of mitochondrial oxidative metabolism (Fig. 8B). In other words, higher TCA cycle and ETC activity would result in a larger increase in mitochondrial membrane potential after oligomycin treatment.

At baseline, VAT T_{regs} had a lower $\Delta\Psi_m$ at ZT0 than at ZT12, as measured by tetramethylrhodamine ethyl ester (TMRE) labeling (Fig. 8C), unlike splenic T_{regs}, wherein the $\Delta\Psi_m$ remained constant (Fig. 8D). The lower $\Delta\Psi_m$ at ZT0 reflected greater oxidative phosphorylation, because inhibition by 1 μM oligomycin induced a greater increase in membrane potential in VAT T_{regs} at ZT0 than at ZT12 (Fig. 8E); in contrast, splenic T_{regs} responded similarly to oligomycin at the two time points (Fig. 8E). Within ST2$^+$ T_{regs}, the p1 subtype exhibited the most prominent diurnal changes (Fig. 8, F and G).

VAT T_{regs} from $T_{reg}^{Bmal1\Delta}$ mice exhibited a higher baseline $\Delta\Psi_m$ at ZT0 than their counterparts from *Bmal1* WT littermates (Fig. 8H), whereas such differences were not observed in the spleen (Fig. 8I). These $\Delta\Psi_m$ differences translated into a greater response to oligomycin in *Bmal1* WT than in *Bmal1* Δ VAT T_{regs}, but not in the corresponding splenic T_{regs} (Fig. 8J). Overall, these findings illustrated VAT-specific diurnal variation in the extent of mitochondrial oxidative metabolism and suggested a role for BMAL1 in promoting ETC activity in VAT T_{regs}.

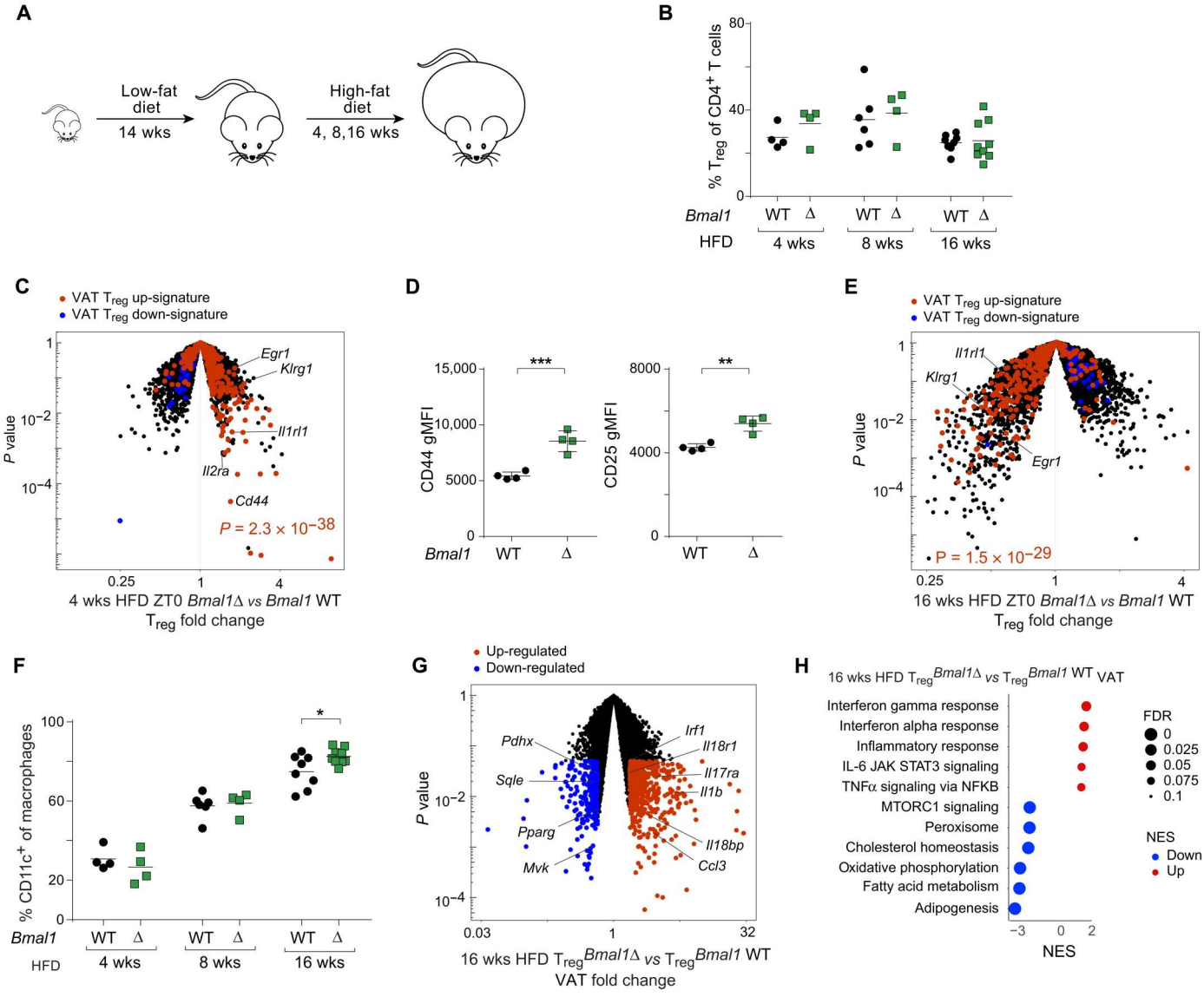

Fig. 7. Accelerated activation but loss of fitness in *Bmal1* Δ T_{regs} during HFD challenge. $T_{reg}^{Bmal1WT}$ and $T_{reg}^{Bmal1\Delta}$ mice were fed a LFD for 14 weeks followed by a HFD for indicated durations; VAT T_{regs} were isolated at ZT0, schematized in (**A**). (**B**) Percentage of VAT T_{regs}. (**C**) Volcano plot of VAT-T_{reg} transcriptome after 4 weeks of HFD overlaid with VAT-T_{reg} signature genes similarly to Fig. 5D. (**D**) gMFI of CD44 (left) and CD25 (right) staining after 4 weeks of HFD. (**E**) Volcano plot of VAT-T_{reg} transcriptome after 16 weeks of HFD, overlaid with VAT-T_{reg} signature genes. (**F**) Fraction of $CD11c^+$ macrophages. (**G**) Volcano plot of whole VAT transcriptome; up- or down-regulated genes with $P \leq 0.05$ and ≥ 1.5 fold change are highlighted; genes of interest are indicated. (**H**) Gene set enrichment analysis (GSEA) of whole VAT transcriptome. For flow cytometric data, $^*P \leq 0.05$, $^{**}P \leq 0.01$, and $^{***}P \leq 0.001$ according to Student's *t* test. Data representative of or pooled from at least two experiments. NES, normalized enrichment score. Flow cytometric gating strategies for all quantified or isolated cell types can be found in fig. S7.

DISCUSSION

It has been reported that the adaptive immune response is unaffected by the cell-intrinsic clock (*12*). However, that study focused on lymphocytes within lymphoid organs, and we found that the transcriptomes of T_{regs} within nonlymphoid, compared with lymphoid, tissues were enriched in pathways associated with circadian rhythms (*1*, *2*). Here, we showed that genes encoding core components of the cell-intrinsic clock were rhythmically expressed in VAT, but not splenic, T_{regs}. T_{reg}-specific mutations of core-clock genes affected VAT, but not splenic, T_{reg} activation, metabolism, and, ultimately, fitness. These differences had organismal consequences: For example, the cell-intrinsic clock enabled VAT T_{regs} to enforce a diurnal rhythm in eVAT lipolysis.

As T_{regs} refine their phenotype in various tissues, they become more activated and adapt their cellular metabolism to their specific locale (*1*). There is past and current evidence that both of these processes fall under circadian control. T cells isolated at different ZTs are differentially sensitive to TCR stimulation (*36*, *37*). Murine $CD8^+$ T cells isolated during the day are more robustly activated after recognition of cognate antigen in vitro and exhibit a diurnal variation in their activation after DC-mediated vaccination in vivo (*37*). BMAL1 restrained VAT, but not splenic, T_{reg} activation,

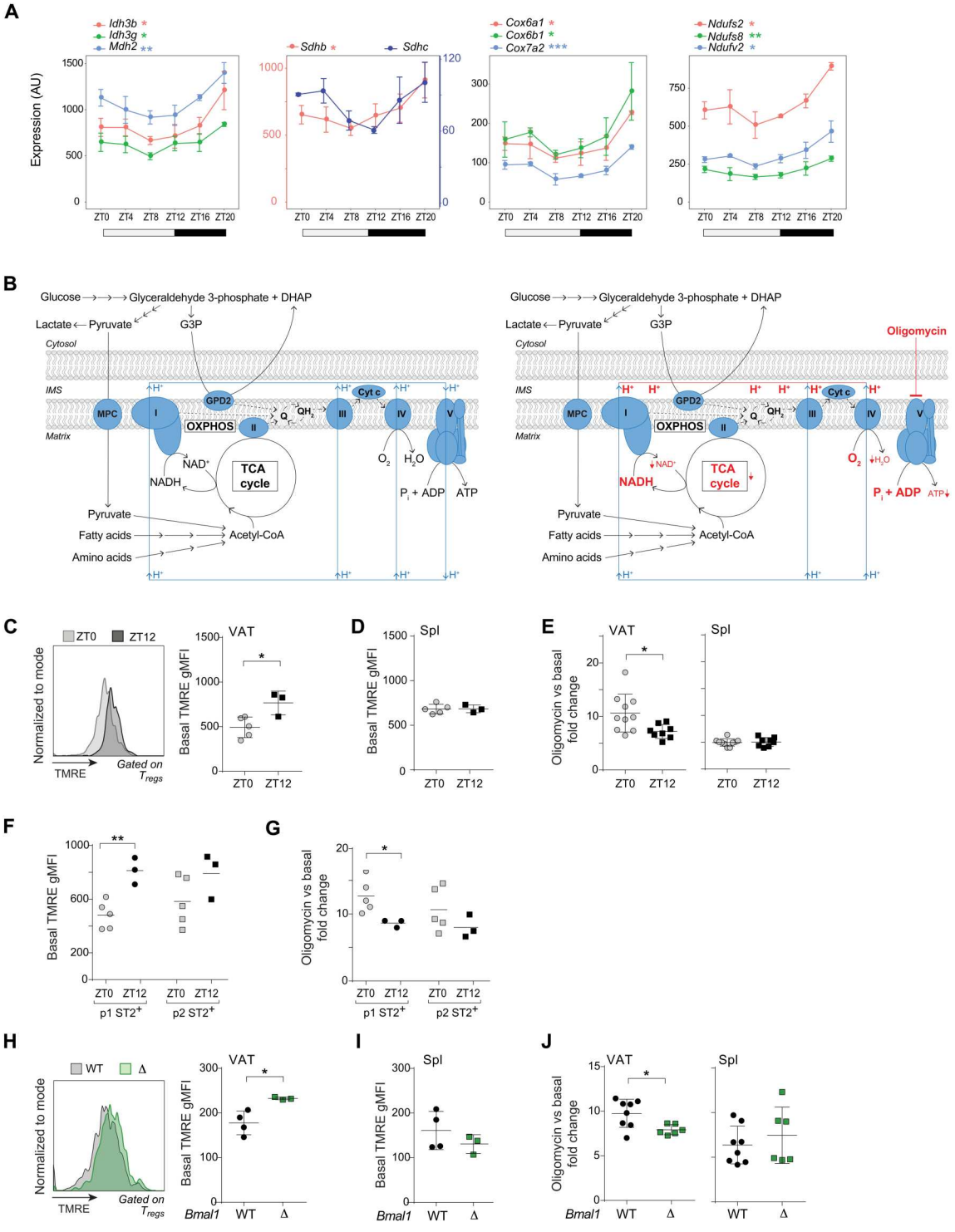

Fig. 8. Circadian regulation of mitochondrial ETC activity. (**A**) Circadian expression profiles of rhythmically expressed genes in the oxidative phosphorylation and TCA cycle pathways. RNA-seq data from Fig. 2. (**B**) Schematic of mitochondrial membrane potential at baseline (left) and after inhibition of complex V by oligomycin (right). Red color emphasizes changes after oligomycin inhibition. (**C** and **D**) Basal mitochondrial membrane potential measured by TMRE at ZT0 and ZT12 in VAT (C) and splenic (D) T_{regs}. (**E**) VAT and splenic T_{reg} responses to oligomycin. Ratio calculated as post-oligomycin gMFI/basal gMFI. (**F**) Basal TMRE in p1 $ST2^+$ ($CD69^{hi}$ $ST2^+$) and p2 $ST2^+$ ($CD69^{lo}$ $ST2^+$) VAT T_{regs} at ZT0 and ZT12; (**G**) their response to oligomycin. (**H** and **I**) Basal mitochondrial membrane potential of *Bmal1* WT and *Bmal1* Δ VAT (H) and splenic (I) T_{regs} at ZT0. (**J**) VAT and splenic T_{reg} responses to oligomycin in $T_{reg}^{Bmal1WT}$ and $T_{reg}^{Bmal1\Delta}$ mice at ZT0. $^*P \leq 0.05$ and $^{**}P \leq 0.01$ by Student's *t* test. Basal TMRE plots: representative of at least two independent experiments. Oligomycin/basal FC: pooled from at least two independent experiments. $n \geq 2$ per condition per experiment. IMS, intermembrane space; OXPHOS, oxidative phosphorylation; FC, fold change. Flow cytometric gating strategies for all quantified or isolated cell types can be found in fig. S7.

similar to its role in other immunocyte populations. Inflammatory cytokine production in macrophages or IL-22 and IL-17 production in ILC3s are heightened after *Bmal1* or *Nr1d1* deletion (*38*–*44*). The brakes on cell activation imposed by BMAL1 in multiple immunocyte lineages that lack TCRs also suggest that the NF-κB signaling pathway might be a primary target of circadian regulation. *Bmal1* deletion heightens NF-κB signaling in macrophages (*38*) and intestinal epithelial cells (*45*).

Many of the rhythmically expressed genes in VAT T_{regs} belonged to metabolic pathways. Our results evidenced a diurnal variation in the TCA cycle and in ETC activity. Rhythms in mitochondrial ETC activity can originate from several processes. For instance, mitochondria undergo diurnal cycles of fusion and fission (*46*–*48*), which modulate the efficiency of ATP production. Fused mitochondria, which are more efficient at producing ATP, occur early in the day (*46*–*49*) and are associated with a heightened mitochondrial oxygen consumption rate and ATP production (*47*, *48*). In VAT T_{regs}, the timing of increased oxidative metabolism coincided with the period of heightened activation state to potentially meet an elevated energy demand. These variations were not present in splenic T_{regs}, highlighting the different metabolic needs of their VAT-T_{reg} counterparts.

In the absence of these and presumably other temporal modulations, VAT T_{regs} lost fitness in competitive transfers, in female T_{reg}^{Bmal1} heterozygotes, and in response to HFD challenge. The reduced fitness resulted from disruption of the core-clock program rather than loss of BMAL1 expression per se, because adoptive transfer of either *Bmal1* or *Nr1d1* Δ T_{regs} led to loss of fitness. Some of the phenotypes in $T_{reg}^{Bmal1\Delta}$ mice might be attributable to other core-clock proteins, such as REV-ERBα, whose expression was significantly altered by loss of BMAL1. The constitutively heightened activation state in Bmal1-deficient T_{regs} suggests dysregulation of the NF-κB signaling pathway, which is intimately related to apoptosis and necrosis. The upstream regulators of NF-κB signaling serve a second, less recognized, function as cell death checkpoints, and NF-κB target genes are known to regulate cell death [reviewed in (*50*, *51*)]. However, the in vivo signals that result in cell death instead of prosurvival signaling by NF-κB in VAT T_{regs} after competitive transfer remain undefined. Furthermore, ETC activity appeared dampened in *Bmal1* Δ VAT T_{regs} and might contribute to the loss of fitness. BMAL1 promotes mitochondrial oxidative metabolism (*42*, *46*, *52*). An inefficient mitochondrial respiration in the absence of BMAL1 increases the production of reactive oxygen species (ROS) (*53*), and ROS exhibits circadian rhythmicity (*41*, *42*, *47*). Poorly optimized mitochondrial function can impair T_{reg} fitness and function, as has been shown in other reports (*54*–*58*).

We uncovered a role for VAT T_{regs} in regulating diurnal lipolysis of the adipose tissue, which requires BMAL1 expression in T_{regs}. NE-induced lipolysis is an important mechanism for providing nutrients during states of energy deprivation (*59*), but excessive lipolysis recruits inflammatory infiltrates to the adipose tissue (*60*, *61*). Thus, adipocyte lipolysis is highly regulated. In mice, lipolysis peaks near ZT0 (*31*), and we recapitulated these findings in vitro: VAT explants isolated at ZT0 resisted further NE stimulation compared with those taken at ZT12. We found that $ST2^+$ T_{regs}, in particular the p1 subtype, suppressed lipolysis in lean animals, and rhythmic lipolysis was disrupted in DT-treated Foxp3-DTR^+ mice and in $T_{reg}^{Bmal1\Delta}$ animals. It seems likely that VAT T_{regs} regulate lipolysis by controlling the inflammatory tenor of the adipose tissue, because cytokines such as TNF-α induce lipolysis (*62*, *63*). Alternatively, T_{regs} might control other VAT immunocytes that modulate sympathetic nervous signaling, such as macrophages (*32*, *64*). Last, VAT T_{regs} might control the sympathetic tone directly through an unknown mechanism. That VAT T_{regs} enforce diurnal lipolysis is consistent with their role in promoting metabolic homeostasis in VAT (*14*, *16*, *17*).

It is unclear how VAT T_{regs} are entrained by circadian rhythms. Identifying specific signals that entrain them, or nonneuronal cells in general, remains an important goal in the field. Hormonal, neuronal, and metabolic signals are drivers of some of the mechanisms [reviewed in (*6*)]. TCR activation up-regulates the expression of core-clock genes such as *Bmal1* and *Nfil3* (11, 65) and thus might kick-start the cell-intrinsic clock program. Metabolic cues such as insulin signaling (*67*) might also entrain resident immunocytes. Given the diurnal lipolysis of adipose tissue, whether lipid species also provide entrainment cues to VAT T_{regs} is an intriguing possibility.

Although we did not find most core-clock genes to be significantly rhythmic in splenic T_{regs}, it remains possible that a more frequent and prolonged sampling, for instance, over 48 hours with a 2-hour sampling interval, might detect weak rhythmicity in the expression of other core-clock genes. Nonetheless, other studies have noted a similarly weak rhythmicity in splenocytes (*12*, *13*). Rhythmicity in VAT T_{regs} entailed changes on the order of twofold, which is less than what has been observed with some cell types, such as hepatocytes, but is similar to observations on other immunocytes (*68*, *69*). Last, because of the very low number of VAT T_{regs} per mouse, we could not perform metabolomics or metabolite-tracing experiments to pinpoint the specific metabolic reactions under diurnal control.

Tissue microenvironments undergo significant changes throughout the day. The elevated rhythmicity of core-clock gene expression provides a molecular mechanism for VAT T_{regs} to synchronize and adapt to the changing tissue environment. An improved understanding of the diurnal behaviors of tissue T_{regs} might help maximize the efficacies of T_{reg}-based immunotherapeutic strategies.

MATERIALS AND METHODS

Study design

This study aimed to establish to what extent circadian rhythms occur in T_{regs} in VAT versus the spleen and how important it is. To that end, we performed transcriptomic profiling by population-level and single-cell RNA sequencing over circadian time as well as cytofluorimetry-based metabolic assays in C57BL/6 and mutant littermates lacking core-clock components.

Mice

C57BL/6 (B6), B6.CD45.1 (stock number 002014, B6.SJL-Ptprca Pepcb/BoyJ), and $Bmal1^{flox/flox}$ (stock number 007668, B6.129S4(Cg)-Arntltm1Weit/J) mice were obtained from the Jackson Laboratory. $Nr1d1^{flox/flox}$ mice have been reported (University of Pennsylvania) (*70*). Foxp3-Ires GFP.hDTR mice were obtained from A. Rudensky (Memorial Sloan Kettering Cancer Center). The B6.*Foxp3-Ires GFP* (*71*), B6.*Foxp3-Cre.YFP* (*72*), and VAT TCR-tg lines (*18*) have been described. Mice lacking *Bmal1* or

Nr1d1 specifically in T_{regs} were generated by crossing B6.*Foxp3-Cre.YFP* mice with the respective flox strains and are typically referred to in the text as $T_{reg}^{Bmal1\Delta}$ or $T_{reg}^{Nr1d1\Delta}$ For transfer experiments, knockout donor strains were generated by crossing B6.*Foxp3-Cre.YFP*.CD45.2$^+$ mice with VAT TCR-tg mice and either the *Bmal1*$^{flox/flox}$ or *Nr1d1*$^{flox/flox}$ strain to obtain *Foxp3-Cre.YFP*.CD45.2$^+$.TCR-tg$^+$ *Bmal1*$^{flox/flox}$ or *Nr1d1*$^{flox/flox}$ offspring. Female heterozygous Cre strains were generated by crossing *Foxp3-Cre.YFP*$^{+/+}$*Bmal1*$^{flox/flox}$ with *Bmal1*$^{flox/flox}$ mice. WT donor strains were obtained by crossing B6.*Foxp3-Cre.YFP* mice with B6.CD45.1 and VAT TCR-tg mice to obtain *Foxp3-CreYFP*.CD45.1$^+$.TCR-tg$^+$ offspring. Recipients were generated by crossing B6.*Foxp3-Cre.YFP* with B6.CD45.1 to obtain *Foxp3-Cre.YFP*.CD45.1/2$^+$ offspring. Appropriate littermate controls were always used except for transfer experiments, where cohoused donors of similar age were used. All animals were housed in specific pathogen–free facilities at Harvard Medical School's Center for Animal Resources and Comparative Medicine. All experiments were performed under protocols approved by the Harvard Medical School Institutional Animal Care and Use Committee (protocol no. IS00001257).

Mice were housed under a strict 12-hour light/12-hour dark cycle. In some experiments, they were entrained in a reverse light cycle room for a minimum of 14 days with a 12-hour light/12-hour dark cycle, which enabled simultaneous tissue collection from mice at different circadian time points. To assess adaptation to reverse light cycle, we housed mice individually with unrestricted access to running wheels equipped with activity tracking (Columbus Instruments). Wheel revolutions were recorded in each cage every 10 s, and cumulative wheel turns from all mice were plotted.

Unless otherwise noted, weaned mice were fed a low-fat diet chow (no. 5053, Picolab Rodent Diet 20; 13% kcal fat) ad libitum. For HFD experiments, mice were fed a low-fat diet chow (no. 5053) ad libitum until 14 weeks of age and then fed an HFD (Open Source Diet D12492; 60% kcal fat) ad libitum for 4, 8, or 16 weeks.

Tissue preparations for flow cytometry and cell sorting

Tissue preparation has been previously described with slight modifications (*29*). Briefly, male mice were euthanized by CO_2. eVAT and spleen were excised and placed in Dulbecco's modified Eagle's medium (DMEM) containing 2% fetal bovine serum (FBS) and 10 mM Hepes (referred to as sorting buffer). VAT depots were minced with scissors and incubated with sorting buffer containing collagenase type II (1.5 mg/ml; Sigma-Aldrich) at 37°C for 20 min. The adipocyte layer was removed after centrifugation at 420*g*. Red blood cells were lysed by ACK lysing buffer (Gibco). Spleen and lymph nodes were mechanically dissociated by mashing against a 40-μm filter, followed by red blood cell removal by ACK lysis. For liver, lung, and kidney preparations, excised tissues were minced with scissors and incubated in 1% fetal calf serum DMEM containing collagenase IV (0.5 mg/ml; Gibco) and deoxyribonuclease I (150 μg/ml; Sigma-Aldrich) at 37°C for 30 to 45 min. Digested tissues were filtered and washed. For liver and kidney, leukocytes were enriched by centrifugation (10 min at 800*g*) with 36% Percoll (GE Healthcare).

For surface-antigen staining, single-cell suspensions were incubated in phosphate-buffered saline (PBS) containing live/dead stain and surface antibodies for 10 min on ice, followed by washes in sorting buffer. For intracellular staining, single-cell suspensions were fixed in eBioscience Fix/Perm buffer for 20 to 30 min at room temperature, followed by permeabilization in eBioscience permeabilization buffer. Cells were stained with intracellular antibodies for 30 min at room temperature, followed by washes with permeabilization buffer.

The following antibodies were used: anti-mouse CD4 (GK1.5), CD8α (53-6.7), CD11b (M1/70), CD11c (N418), CD19 (6D5), CD39 (Duha59), CD45 (30-F11), CD45.1 (A20), CD45.2 (104), CD62L (MEL-14), CD69 (H1.2F3), Il18r/CD218α (BG/IL18RA), CD44 (IM7), Il17r/CD127 (A7R34), CD206 (C068C2), Ly6c (HK1.4), F4/80 (BM8), and I-A/I-E (M5/114.15.2) all from BioLegend; CD25 (PC61), TCRβ (H57–597), and Ki67 (B56) from BD Bioscience; Foxp3 (FJK-16s), Il33R/ST2 (RMST2–2), and Klrg1 (2F1) from Thermo Fisher Scientific. Live/Dead fixable viability dye yellow, near-infrared, or ultraviolet (Thermo Fisher Scientific) was used to distinguish live and dead cells. Typically, T_{regs} were defined as CD45$^+$ TCRβ$^+$ CD4$^+$ Foxp3$^+$. For cell sorting, T_{regs} were defined as CD45$^+$ Tcrb$^+$ CD4$^+$ YFP$^+$ CD8α$^-$ CD11b$^-$ CD11c$^-$ CD19$^-$ DAPI$^-$ unless otherwise specified.

RNA sequencing

RNA-seq was performed as described at www.immgen.org. A total of 1000 T_{regs} were double-sorted directly into 5 μl of TCL buffer (Qiagen) containing 1% β-mercaptoethanol (Sigma-Aldrich). For adoptive transfer experiments, 500 cells were double-sorted. Smart-seq2 libraries were prepared and sequenced as previously described (*73*) using the Broad Genomics Platform. Briefly, RNA was captured and purified using RNAClean XP beads (Beckman Coulter). Polyadenylated mRNA was selected using an anchored oligo(dT) primer (50-AAGCAGTGGTATCAACGCAGAGTACT30VN-30) and converted to complementary DNA (cDNA) by reverse transcription. Limited PCR amplification was performed on the first-strand cDNA followed by Tn5 transposon–based fragmentation using the Nextera XT DNA Library Preparation Kit (Illumina). Samples were PCR-amplified for 12 cycles using barcoded primers such that each sample carried a specific combination of eight base Illumina P5 and P7 barcodes for subsequent pooling and sequencing. Paired-end sequencing was performed on an Illumina NextSeq 500 using 2 × 38–base pair reads with no further trimming. Reads were aligned to the mouse genome (GENCODE GRCm38/mm10 primary assembly and gene annotations vM16; www.gencodegenes.org/mouse/release_M16.html) with STAR 2.5.4a (https://github.com/alexdobin/STAR/releases). Ribosomal RNA gene annotations were removed from the GTF (general transfer format) file. Gene-level quantification was calculated by featureCounts (http://subread.sourceforge.net/). Raw read count tables were normalized by the median of ratios method with the DESeq2 package from Bioconductor (https://bioconductor.org/packages/release/bioc/html/DESeq2.html) and then converted to GCT and CLS format. Samples with fewer than 1 million uniquely mapped reads or with fewer than 8000 genes over 10 reads were considered low quality and removed, followed by further screening for contamination by using known cell type–specific transcripts. Biological replicates with a poor Pearson's correlation (<0.9) were removed. Genes with fewer than 10 reads across samples or a high coefficient of variation (typically >0.6) were removed. Differential gene expression analysis was performed using EdgeR (*74*); differentially expressed genes were defined as $P \leq 0.05$ according

to quasi-likelihood *F* test. For pathway enrichment analysis, differentially expressed genes were analyzed by ingenuity pathway analysis (Qiagen, https://digitalinsights.qiagen.com/products-overview/discovery-insights-portfolio/analysis-and-visualization/qiagen-ipa/) (*75*), gene set enrichment analysis (*76*), or EnrichR (*77*, *78*). Enriched pathways were defined as false discovery rate (FDR) ≤ 0.05. In some cases, previously established signatures were tested for enrichment in our dataset, where significant enrichment was defined as $P \leq 0.05$ according to Fisher's exact test.

For whole-tissue RNA-seq, RNA was extracted from VAT using the RNeasy Lipid Tissue Mini Kit following the manufacturer's protocol (Qiagen). Two nanograms of RNA was added into 5 μl of TCL buffer (Qiagen) containing 1% β-mercaptoethanol (Sigma-Aldrich) and sequenced as above.

RT-PCR

RNA was extracted from 100,000 sorted splenocytes using TRIzol (Invitrogen) following the manufacturer's protocol. cDNA synthesis was performed using a Maxima H Minus Reverse Transcriptase kit (Thermo Fisher Scientific). qPCR was run on a QuantStudio 5 Real-Time PCR System (Applied Biosystems). The expression of *Bmal1* was calculated by the $2^{-\Delta\Delta Ct}$ method relative to the expression of the ribosomal subunit *36b4* (*Rplp0*). Primer sequences are as follows: *Bmal1*, AGGATCAAGAATGCAAGGGAGG (F) and TGAAACTGTTCATTTTGTCCCGA (R); *Rplp0*, GGAGTGACATCGTCTTTAAACCCC (F) and TCTGCTCCCACAATGAAGCA (R).

Adoptive transfers

Cells from 6- to 8-week-old male donors were pooled from spleen and peripheral lymph nodes, followed by enrichment for $CD4^+$ cells using Dynabeads untouched Mouse CD4 (Thermo Fisher Scientific). Cells were single-sorted for YFP^+ T_{regs}. For the competitive transfer experiments, a 1:1 mix of 250,000 donor T_{regs} from WT or knockout donors (500,000 total T_{regs}) were resuspended in PBS and intravenously injected via the tail vein into 8- to 10-week-old male recipients. Donor and recipient mice were fed a low-fat diet chow with 21% kcal fat (no. 5058, Picolab Rodent Diet 20).

scRNA-seq

A total of 34,000 VAT and 32,000 splenic $CD4^+$ T cells were sorted and multiplexed using TotalSeq hashing antibodies (BioLegend). Cell encapsulation, RNA isolation, and hash library construction and sequencing were performed by Broad Institute Genomic Services using the 10X Genomics platform. Samples were processed using 3′ v3.1 chemistry, and hashed cells were loaded onto one lane. cDNA and gene expression libraries were constructed following the manufacturer's instructions (10X Genomics). Gene expression libraries were sequenced on HiSeq X. Samples were demultiplexed using cellranger v6.0, and hash libraries were processed using cite-seq-count (https://hoohm.github.io/CITE-seq-Count/).

Data analysis was performed following the Seurat v3 pipeline (*79*). Low-quality cells were removed and were defined as those with fewer than 700 or more than 3000 unique genes as well as those with >10% mitochondrial gene reads. Clusters of proliferating cells were also removed. Non-$CD4^+$ T cell contaminants were removed using well-known cell identity markers. Clustering, dimensionality reduction onto UMAP, differential gene expression, and visualization were performed using the built-in functions of Seurat v3. Density distributions were calculated using two-dimensional kernel density estimation.

RNA velocity was performed as previously described (*27*). Briefly, the spliced and unspliced counts were calculated from the original sequencing data using the RNA velocity package (*26*). The spliced and unspliced expression matrices were then integrated into the single-cell data matrix, and the scvelo package was used to calculate the velocity vectors using the dynamical model of transcriptional dynamics and splicing kinetics. The calculated velocity vectors were then projected onto the UMAP embedding calculated during the scRNA-seq analysis.

Lipolysis assays

The in vitro lipolysis assay was adapted from previous studies (*32*, *33*, *80*). Briefly, about 20 mg of eVAT was excised into 200 μl of glucose DMEM (1 g/liter; Gibco) supplemented with 10 mM Hepes, 2% fatty acid–free bovine serum albumin (Sigma-Aldrich), and 5 μM Triacsin C (Sigma-Aldrich) (collectively referred to as "lipolysis buffer"), with or without NE (A0937 Sigma-Aldrich) for 1 hour at 37°C. Explants were then transferred into fresh lipolysis buffer with or without NE for an additional hour, and the supernatant was collected for glycerol quantification following the manufacturer's protocol (SGA1, Zenbio). To quantify protein content, we placed the fat pad into 1 ml of chloroform:methanol (2:1, v/v) with 1% glacial acetic acid (extraction solution) for 1 hour at 37°C while rotating and then incubated the material in 500 μl of 0.3 N NaOH with 0.1% SDS in dH_2O (lysis buffer) overnight at 55°C. The lysis buffer supernatant was taken for protein quantification using the Pierce BCA assay following the manufacturer's protocol (Thermo Fisher Scientific). Glycerol release rate was expressed as micromolar glycerol per milligram of protein per hour.

For induction of lipolysis in vivo, CL316,243 (1 mg/kg; Sigma-Aldrich) was intraperitoneally injected. Serum was collected via the tail vein using nonheparinized capillary tubes (Thermo Fisher Scientific) and was allowed to clot at room temperature for 15 min. After centrifugation at 2000*g* for 15 min, the supernatant was assayed for free fatty acid or glycerol levels following the manufacturer's protocol (GFA-1 Zenbio). Foxp3-DTR^+ mice was intraperitoneally injected with DT (20 ng/g) once per day, at ZT0 or ZT12, for three consecutive days.

Organismal metabolism

Organismal metabolism was assessed by the glucose tolerance test (GTT) and insulin tolerance test (ITT). For the GTT, mice were fasted for 5 hours and acclimatized to the experiment room for 45 min, followed by intraperitoneal injection of glucose (1 g/kg). Glucose levels were then measured from tail vein blood at 0, 20, 40, 60, 90, and 120 min after the glucose injection. For ITT, mice were fasted for 4 hours, followed by 45 min of acclimatization to the experiment room. They were intraperitoneally injected with 0.6 U/kg (Humulin R U-100 from Eli Lilly), followed by glucose level measurements at 0, 20, 40, 60, 90, and 120 min after injection. Blood glucose levels were measured using a Contour glucose meter.

Cellular metabolism

Mitochondrial membrane potential was measured using TMRE from Thermo Fisher Scientific. Single-cell suspensions were stained with surface antibodies as described above and washed in sorting buffer. Cells were then incubated in a round-bottom 96-

well tissue-culture plate (Corning) in 100 μl of DMEM + 2% FBS + 10 mM Hepes + 2 mM glutamine at 37°C for 30 min. Where applicable, cells were treated with 1 μM oligomycin (delivered at 3× concentration in 50 μl) at 37°C for 10 min. Last, cells were stained with 100 μM TMRE (delivered at 4× in 50 μl) at 37°C for 20 min. Cells were spun down and resuspended in cold FACS buffer without any further washes before immediate acquisition on the flow cytometer.

Statistical analyses

Data are routinely shown as mean ± SD. Unless stated otherwise, statistical significance was determined by two-tailed Student's *t* test using GraphPad Prism 9.0. $*P < 0.05$, $**P < 0.01$, and $***P < 0001$. A value of more than three SDs from the mean was adopted as the criterion to exclude outliers. Independent replicate experiments were typically performed with at least two biological replicates per group. Circadian rhythmicity of gene expression was assessed using JTK_CYCLE (*81*). Rhythmic genes were defined as $P \leq 0.05$, gene expression ≥20, and period ≥16 hours. Time of peak expression was determined by JTK_CYCLE.

Supplementary Materials

This PDF file includes:
Figs. S1 to S7

Other Supplementary Material for this manuscript includes the following:
Table S1
Data file S1

View/request a protocol for this paper from *Bio-protocol*.

REFERENCES AND NOTES

1. A. R. Muñoz-Rojas, D. Mathis, Tissue regulatory T cells: Regulatory chameleons. *Nat. Rev. Immunol.* **21**, 597–611 (2021).
2. J. R. Dispirito, D. Zemmour, D. Ramanan, J. Cho, R. Zilionis, A. M. Klein, C. Benoist, D. Mathis, Molecular diversification of regulatory T cells in nonlymphoid tissues. *Sci. Immunol.* **3**, eaat5861 (2018).
3. J. S. Takahashi, Transcriptional architecture of the mammalian circadian clock. *Nat. Rev. Genet.* **18**, 164–179 (2017).
4. C. Dibner, U. Schibler, U. Albrecht, The mammalian circadian timing system: Organization and coordination of central and peripheral clocks. *Annu. Rev. Physiol.* **72**, 517–549 (2010).
5. C. Saini, D. M. Suter, A. Liani, P. Gos, U. Schibler, The mammalian circadian timing system: Synchronization of peripheral clocks. *Cold Spring Harb. Symp. Quant. Biol.* **76**, 39–47 (2011).
6. U. Schibler, I. Gotic, C. Saini, P. Gos, T. Curie, Y. Emmenegger, F. Sinturel, P. Gosselin, A. Gerber, F. Fleury-Olela, G. Rando, M. Demarque, P. Franken, Clock-talk: Interactions between central and peripheral circadian oscillators in mammals. *Cold Spring Harb. Symp. Quant. Biol.* **80**, 223–232 (2015).
7. K. Suzuki, Y. Hayano, A. Nakai, F. Furuta, M. Noda, Adrenergic control of the adaptive immune response by diurnal lymphocyte recirculation through lymph nodes. *J. Exp. Med.* **213**, 2567–2574 (2016).
8. D. Druzd, O. Matveeva, L. Ince, U. Harrison, W. He, C. Schmal, H. Herzel, A. H. Tsang, N. Kawakami, A. Leliavski, O. Uhl, L. Yao, L. E. Sander, C.-S. Chen, K. Kraus, A. de Juan, S. M. Hergenhan, M. Ehlers, B. Koletzko, R. Haas, W. Solbach, H. Oster, C. Scheiermann, Lymphocyte circadian clocks control lymph node trafficking and adaptive immune responses. *Immunity* **46**, 120–132 (2017).
9. A. Shimba, G. Cui, S. Tani-ichi, M. Ogawa, S. Abe, F. Okazaki, S. Kitano, H. Miyachi, H. Yamada, T. Hara, Y. Yoshikai, T. Nagasawa, G. Schütz, K. Ikuta, Glucocorticoids drive diurnal oscillations in T cell distribution and responses by inducing interleukin-7 receptor and CXCR4. *Immunity* **48**, 286–298.e6 (2018).
10. W. He, S. Holtkamp, S. M. Hergenhan, K. Kraus, A. de Juan, J. Weber, P. Bradfield, J. M. P. Grenier, J. Pelletier, D. Druzd, C.-S. Chen, L. M. Ince, S. Bierschenk, R. Pick, M. Sperandio, M. Aurrand-Lions, C. Scheiermann, Circadian expression of migratory factors establishes lineage-specific signatures that guide the homing of leukocyte subsets to tissues. *Immunity* **49**, 1175–1190.e7 (2018).
11. X. Yu, D. Rollins, K. A. Ruhn, J. J. Stubblefield, C. B. Green, M. Kashiwada, P. B. Rothman, J. S. Takahashi, L. V. Hooper, TH17 cell differentiation is regulated by the circadian clock. *Science* **342**, 727–730 (2013).
12. S. Hemmers, A. Y. Rudensky, The cell-intrinsic circadian clock is dispensable for lymphocyte differentiation and function. *Cell Rep.* **11**, 1339–1349 (2015).
13. L. E. Hand, K. J. Gray, S. H. Dickson, D. A. Simpkins, D. W. Ray, J. E. Konkel, M. R. Hepworth, J. E. Gibbs, Regulatory T cells confer a circadian signature on inflammatory arthritis. *Nat. Commun.* **11**, 1658 (2020).
14. M. Feuerer, L. Herrero, D. Cipolletta, A. Naaz, J. Wong, A. Nayer, J. Lee, A. B. Goldfine, C. Benoist, S. Shoelson, D. Mathis, Lean, but not obese, fat is enriched for a unique population of regulatory T cells that affect metabolic parameters. *Nat. Med.* **15**, 930–939 (2009).
15. D. Kolodin, N. van Panhuys, C. Li, A. M. Magnuson, D. Cipolletta, C. M. Miller, A. Wagers, R. N. Germain, C. Benoist, D. Mathis, Antigen- and cytokine-driven accumulation of regulatory T cells in visceral adipose tissue of lean mice. *Cell Metab.* **21**, 543–557 (2015).
16. D. Cipolletta, M. Feuerer, A. Li, N. Kamei, J. Lee, S. E. Shoelson, C. Benoist, D. Mathis, PPAR-γ is a major driver of the accumulation and phenotype of adipose tissue Treg cells. *Nature* **486**, 549–553 (2012).
17. A. Vasanthakumar, K. Moro, A. Xin, Y. Liao, R. Gloury, S. Kawamoto, S. Fagarasan, L. A. Mielke, S. Afshar-Sterle, S. L. Masters, S. Nakae, H. Saito, J. M. Wentworth, P. Li, W. Liao, W. J. Leonard, G. K. Smyth, W. Shi, S. L. Nutt, S. Koyasu, A. Kallies, The transcriptional regulators IRF4, BATF and IL-33 orchestrate development and maintenance of adipose tissue-resident regulatory T cells. *Nat. Immunol.* **16**, 276–285 (2015).
18. C. Li, J. R. DiSpirito, D. Zemmour, R. G. Spallanzani, W. Kuswanto, C. Benoist, D. Mathis, TCR transgenic mice reveal stepwise, multi-site acquisition of the distinctive fat-Treg phenotype. *Cell* **174**, 285–299.e12 (2018).
19. D. Burzyn, W. Kuswanto, D. Kolodin, J. L. Shadrach, M. Cerletti, Y. Jang, E. Sefik, T. G. Tan, A. J. Wagers, C. Benoist, D. Mathis, A special population of regulatory T cells potentiates muscle repair. *Cell* **155**, 1282–1295 (2013).
20. E. Sefik, N. Geva-Zatorsky, S. Oh, L. Konnikova, D. Zemmour, A. M. McGuire, D. Burzyn, A. Ortiz-Lopez, M. Lobera, J. Yang, S. Ghosh, A. Earl, S. B. Snapper, R. Jupp, D. Kasper, D. Mathis, C. Benoist, Individual intestinal symbionts induce a distinct population of RORγ$^+$ regulatory T cells. *Science* **349**, 993–997 (2015).
21. S. Masri, P. Rigor, M. Cervantes, N. Ceglia, C. Sebastian, C. Xiao, M. Roqueta-Rivera, C. Deng, T. F. Osborne, R. Mostoslavsky, P. Baldi, P. Sassone-Corsi, Partitioning circadian transcription by SIRT6 leads to segregated control of cellular metabolism. *Cell* **158**, 659–672 (2014).
22. N. Ceglia, Y. Liu, S. Chen, F. Agostinelli, K. Eckel-Mahan, P. Sassone-Corsi, P. Baldi, CircadiOmics: Circadian omic web portal. *Nucleic Acids Res.* **46**, W157–W162 (2018).
23. L. S. Mure, H. D. le, G. Benegiamo, M. W. Chang, L. Rios, N. Jillani, M. Ngotho, T. Kariuki, O. Dkhissi-Benyahya, H. M. Cooper, S. Panda, Diurnal transcriptome atlas of a primate across major neural and peripheral tissues. *Science* **359**, eaao0318 (2018).
24. K. F. Storch, C. Paz, J. Signorovitch, E. Raviola, B. Pawlyk, T. Li, C. J. Weitz, Intrinsic circadian clock of the mammalian retina: Importance for retinal processing of visual information. *Cell* **130**, 730–741 (2007).
25. K. Eckel-Mahan, P. Sassone-Corsi, Phenotyping circadian rhythms in mice. *Curr. Protoc. Mouse Biol.* **5**, 271–281 (2015).
26. G. La Manno, R. Soldatov, A. Zeisel, E. Braun, H. Hochgerner, V. Petukhov, K. Lidschreiber, M. E. Kastriti, P. Lönnerberg, A. Furlan, J. Fan, L. E. Borm, Z. Liu, D. van Bruggen, J. Guo, X. He, R. Barker, E. Sundström, G. Castelo-Branco, P. Cramer, I. Adameyko, S. Linnarsson, P. V. Kharchenko, RNA velocity of single cells. *Nature* **560**, 494–498 (2018).
27. V. Bergen, M. Lange, S. Peidli, F. A. Wolf, F. J. Theis, Generalizing RNA velocity to transient cell states through dynamical modeling. *Nat. Biotechnol.* **38**, 1408–1414 (2020).
28. D. Cipolletta, P. Cohen, B. M. Spiegelman, C. Benoist, D. Mathis, Appearance and disappearance of the mRNA signature characteristic of Treg cells in visceral adipose tissue: Age, diet, and PPARγ effects. *Proc. Natl. Acad. Sci. U.S.A.* **112**, 482–487 (2015).
29. R. G. Spallanzani, D. Zemmour, T. Xiao, T. Jayewickreme, C. Li, P. J. Bryce, C. Benoist, D. Mathis, Distinct immunocyte-promoting and adipocyte-generating stromal components coordinate adipose-tissue immune and metabolic tenors. *Sci. Immunol.* **4**, eaaw3658 (2019).
30. A. Vasanthakumar, D. Chisanga, J. Blume, R. Gloury, K. Britt, D. C. Henstridge, Y. Zhan, S. V. Torres, S. Liene, N. Collins, E. Cao, T. Sidwell, C. Li, R. G. Spallanzani, Y. Liao, P. A. Beavis, T. Gebhardt, N. Trevaskis, S. L. Nutt, J. D. Zajac, R. A. Davey, M. A. Febbraio, D. Mathis, W. Shi, A. Kallies, Sex-specific adipose tissue imprinting of regulatory T cells. *Nature* **579**, 581–585 (2020).
31. A. Shostak, J. Meyer-Kovac, H. Oster, Circadian regulation of lipid mobilization in white adipose tissues. *Diabetes* **62**, 2195–2203 (2013).

32. C. D. Camell, J. Sander, O. Spadaro, A. Lee, K. Y. Nguyen, A. Wing, E. L. Goldberg, Y.-H. Youm, C. W. Brown, J. Elsworth, M. S. Rodeheffer, J. L. Schultze, V. D. Dixit, Inflammasome-driven catecholamine catabolism in macrophages blunts lipolysis during ageing. *Nature* **550**, 119–123 (2017).
33. M. Schweiger, T. O. Eichmann, U. Taschler, R. Zimmermann, R. Zechner, A. Lass, Measurement of lipolysis. *Methods Enzymol.* **538**, 171–193 (2014).
34. D. Patsouris, S. Mandard, P. J. Voshol, P. Escher, N. S. Tan, L. M. Havekes, W. Koenig, W. März, S. Tafuri, W. Wahli, M. Müller, S. Kersten, PPARα governs glycerol metabolism. *J. Clin. Invest.* **114**, 94–103 (2004).
35. C. Li, G. Wang, P. Sivasami, R. N. Ramirez, Y. Zhang, C. Benoist, D. Mathis, Interferon-α-producing plasmacytoid dendritic cells drive the loss of adipose tissue regulatory T cells during obesity. *Cell Metab.* **33**, 1610–1623 (2021).
36. E. E. Fortier, J. Rooney, H. Dardente, M.-P. Hardy, N. Labrecque, N. Cermakian, Circadian variation of the response of T cells to antigen. *J. Immunol.* **187**, 6291–6300 (2011).
37. C. C. Nobis, G. Dubeau Laramée, L. Kervezee, D. Maurice de Sousa, N. Labrecque, N. Cermakian, The circadian clock of CD8 T cells modulates their early response to vaccination and the rhythmicity of related signaling pathways. *Proc. Natl. Acad. Sci. U.S.A.* **116**, 20077–20086 (2019).
38. A. M. Curtis, C. T. Fagundes, G. Yang, E. M. Palsson-McDermott, P. Wochal, A. F. McGettrick, N. H. Foley, J. O. Early, L. Chen, H. Zhang, C. Xue, S. S. Geiger, K. Hokamp, M. P. Reilly, A. N. Coogan, E. Vigorito, G. A. FitzGerald, L. A. J. O'Neill, Circadian control of innate immunity in macrophages by miR-155 targeting Bmal1. *Proc. Natl. Acad. Sci. U.S.A.* **112**, 7231–7236 (2015).
39. Y. Oishi, S. Hayashi, T. Isagawa, M. Oshima, A. Iwama, S. Shimba, H. Okamura, I. Manabe, Bmal1 regulates inflammatory responses in macrophages by modulating enhancer RNA transcription. *Sci. Rep.* **7**, 7086 (2017).
40. C. E. Sutton, C. M. Finlay, M. Raverdeau, J. O. Early, J. DeCourcey, Z. Zaslona, L. A. J. O'Neill, K. H. G. Mills, A. M. Curtis, Loss of the molecular clock in myeloid cells exacerbates T cell-mediated CNS autoimmune disease. *Nat. Commun.* **8**, 1923 (2017).
41. J. O. Early, D. Menon, C. A. Wyse, M. P. Cervantes-Silva, Z. Zaslona, R. G. Carroll, E. Palsson-McDermott, S. Angiari, D. G. Ryan, S. E. Corcoran, G. Timmons, S. S. Geiger, D. J. Fitzpatrick, D. O'Connell, R. J. Xavier, K. Hokamp, L. A. J. O'Neill, A. M. Curtis, Circadian clock protein BMAL1 regulates IL-1β in macrophages via NRF2. *Proc. Natl. Acad. Sci. U.S.A.* **115**, E8460–E8468 (2018).
42. R. K. Alexander, Y.-H. Liou, N. H. Knudsen, K. A. Starost, C. Xu, A. L. Hyde, S. Liu, D. Jacobi, N. S. Liao, C.-H. Lee, Bmal1 integrates mitochondrial metabolism and macrophage activation. *eLife* **9**, e54090 (2020).
43. F. Teng, J. Goc, L. Zhou, C. Chu, M. A. Shah, G. Eberl, G. F. Sonnenberg, A circadian clock is essential for homeostasis of group 3 innate lymphoid cells in the gut. *Sci. Immunol.* **4**, eaax1215 (2019).
44. Q. Wang, M. L. Robinette, C. Billon, P. L. Collins, J. K. Bando, J. L. Fachi, C. Sécca, S. I. Porter, A. Saini, S. Gilfillan, L. A. Solt, E. S. Musiek, E. M. Oltz, T. P. Burris, M. Colonna, Circadian rhythm-dependent and circadian rhythm-independent impacts of the molecular clock on type 3 innate lymphoid cells. *Sci Immunol.* **4**, eaay7501 (2019).
45. A. Mukherji, A. Kobiita, T. Ye, P. Chambon, Homeostasis in intestinal epithelium is orchestrated by the circadian clock and microbiota cues transduced by TLRs. *Cell* **153**, 812–827 (2013).
46. D. Jacobi, S. Liu, K. Burkewitz, N. Kory, N. H. Knudsen, R. K. Alexander, U. Unluturk, X. Li, X. Kong, A. L. Hyde, M. R. Gangl, W. B. Mair, C.-H. Lee, Hepatic Bmal1 regulates rhythmic mitochondrial dynamics and promotes metabolic fitness. *Cell Metab.* **22**, 709–720 (2015).
47. K. Schmitt, A. Grimm, R. Dallmann, B. Oettinghaus, L. M. Restelli, M. Witzig, N. Ishihara, K. Mihara, J. A. Ripperger, U. Albrecht, S. Frank, S. A. Brown, A. Eckert, Circadian control of DRP1 activity regulates mitochondrial dynamics and bioenergetics. *Cell Metab.* **27**, 657–666.e5 (2018).
48. E. J. Collins, M. P. Cervantes-Silva, G. A. Timmons, J. R. O'Siorain, A. M. Curtis, J. M. Hurley, Post-transcriptional circadian regulation in macrophages organizes temporally distinct immunometabolic states. *Genome Res.* **31**, 171–185 (2021).
49. L. Sardon Puig, M. Valera-Alberni, C. Canto, N. J. Pillon, Circadian rhythms and mitochondria: Connecting the dots. *Front. Genet.* **9**, 452 (2018).
50. V. Kondylis, S. Kumari, K. Vlantis, M. Pasparakis, The interplay of IKK, NF-κB and RIPK1 signaling in the regulation of cell death, tissue homeostasis and inflammation. *Immunol. Rev.* **277**, 113–127 (2017).
51. S. Blanchett, I. Boal-Carvalho, S. Layzell, B. Seddon, NF-κB and extrinsic cell death pathways—Entwined do-or-die decisions for T cells. *Trends Immunol.* **42**, 76–88 (2021).
52. C. B. Peek, A. H. Affinati, K. M. Ramsey, H.-Y. Kuo, W. Yu, L. A. Sena, O. Ilkayeva, B. Marcheva, Y. Kobayashi, C. Omura, D. C. Levine, D. J. Bacsik, D. Gius, C. B. Newgard, E. Goetzman, N. S. Chandel, J. M. Denu, M. Mrksich, J. Bass, Circadian clock NAD^+ cycle drives mitochondrial oxidative metabolism in mice. *Science* **342**, 1243417 (2013).
53. M. P. Murphy, How mitochondria produce reactive oxygen species. *Biochem. J.* **417**, 1–13 (2009).
54. N. He, W. Fan, B. Henriquez, R. T. Yu, A. R. Atkins, C. Liddle, Y. Zheng, M. Downes, R. M. Evans, Metabolic control of regulatory T cell (Treg) survival and function by Lkb1. *Proc. Natl. Acad. Sci. U.S.A.* **114**, 12542–12547 (2017).
55. K. Yang, D. B. Blanco, G. Neale, P. Vogel, J. Avila, C. B. Clish, C. Wu, S. Shrestha, S. Rankin, L. Long, A. KC, H. Chi, Homeostatic control of metabolic and functional fitness of Treg cells by LKB1 signalling. *Nature* **548**, 602–606 (2017).
56. S. E. Weinberg, B. D. Singer, E. M. Steinert, C. A. Martinez, M. M. Mehta, I. Martínez-Reyes, P. Gao, K. A. Helmin, H. Abdala-Valencia, L. A. Sena, P. T. Schumacker, L. A. Turka, N. S. Chandel, Mitochondrial complex III is essential for suppressive function of regulatory T cells. *Nature* **565**, 495–499 (2019).
57. U. H. Beier, A. Angelin, T. Akimova, L. Wang, Y. Liu, H. Xiao, M. A. Koike, S. A. Hancock, T. R. Bhatti, R. Han, J. Jiao, S. C. Veasey, C. A. Sims, J. A. Baur, D. C. Wallace, W. W. Hancock, Essential role of mitochondrial energy metabolism in $Foxp3^+$ T-regulatory cell function and allograft survival. *FASEB J.* **29**, 2315–2326 (2015).
58. C. S. Field, F. Baixauli, R. L. Kyle, D. J. Puleston, A. M. Cameron, D. E. Sanin, K. L. Hippen, M. Loschi, G. Thangavelu, M. Corrado, J. Edwards-Hicks, K. M. Grzes, E. J. Pearce, B. R. Blazar, E. L. Pearce, Mitochondrial integrity regulated by lipid metabolism is a cell-intrinsic checkpoint for Treg suppressive function. *Cell Metab.* **31**, 422–437.e5 (2020).
59. R. E. Duncan, M. Ahmadian, K. Jaworski, E. Sarkadi-Nagy, H. S. Sul, Regulation of lipolysis in adipocytes. *Annu. Rev. Nutr.* **27**, 79–101 (2007).
60. A. Kosteli, E. Sugaru, G. Haemmerle, J. F. Martin, J. Lei, R. Zechner, A. W. Ferrante Jr., Weight loss and lipolysis promote a dynamic immune response in murine adipose tissue. *J. Clin. Invest.* **120**, 3466–3479 (2010).
61. R. J. Roth Flach, A. Matevossian, T. E. Akie, K. A. Negrin, M. T. Paul, M. P. Czech, β3-Adrenergic receptor stimulation induces E-selectin-mediated adipose tissue inflammation. *J. Biol. Chem.* **288**, 2882–2892 (2013).
62. R. W. Grant, J. M. Stephens, Fat in flames: Influence of cytokines and pattern recognition receptors on adipocyte lipolysis. *Am. J. Physiol. Endocrinol. Metab.* **309**, E205–E213 (2015).
63. H. H. Zhang, M. Halbleib, F. Ahmad, V. C. Manganiello, A. S. Greenberg, Tumor necrosis factor-alpha stimulates lipolysis in differentiated human adipocytes through activation of extracellular signal-related kinase and elevation of intracellular cAMP. *Diabetes* **51**, 2929–2935 (2002).
64. R. M. Pirzgalska, E. Seixas, J. S. Seidman, V. M. Link, N. M. Sánchez, I. Mahú, R. Mendes, V. Gres, N. Kubasova, I. Morris, B. A. Arús, C. M. Larabee, M. Vasques, F. Tortosa, A. L. Sousa, S. Anandan, E. Tranfield, M. K. Hahn, M. Iannacone, N. J. Spann, C. K. Glass, A. I. Domingos, Sympathetic neuron-associated macrophages contribute to obesity by importing and metabolizing norepinephrine. *Nat. Med.* **23**, 1309–1318 (2017).
65. E. Wakamatsu, D. Mathis, C. Benoist, Convergent and divergent effects of costimulatory molecules in conventional and regulatory $CD4^+$ T cells. *Proc. Natl. Acad. Sci. U.S.A.* **110**, 1023–1028 (2013).
66. A. H. Hassall, *The Microscopic Anatomy of the Human Body: In Health and Disease* (S. Highley, 1846).
67. P. Crosby, R. Hamnett, M. Putker, N. P. Hoyle, M. Reed, C. J. Karam, E. S. Maywood, A. Stangherlin, J. E. Chesham, E. A. Hayter, L. Rosenbrier-Ribeiro, P. Newham, H. Clevers, D. A. Bechtold, J. S. O'Neill, Insulin/IGF-1 drives PERIOD synthesis to entrain circadian rhythms with feeding time. *Cell* **177**, 896–909.e20 (2019).
68. C. Godinho-Silva, R. G. Domingues, M. Rendas, B. Raposo, H. Ribeiro, J. A. da Silva, A. Vieira, R. M. Costa, N. L. Barbosa-Morais, T. Carvalho, H. Veiga-Fernandes, Light-entrained and brain-tuned circadian circuits regulate ILC3s and gut homeostasis. *Nature* **574**, 254–258 (2019).
69. D. Guan, Y. Xiong, T. M. Trinh, Y. Xiao, W. Hu, C. Jiang, P. Dierickx, C. Jang, J. D. Rabinowitz, M. A. Lazar, The hepatocyte clock and feeding control chronophysiology of multiple liver cell types. *Science* **369**, 1388–1394 (2020).
70. P. Dierickx, M. J. Emmett, C. Jiang, K. Uehara, M. Liu, M. Adlanmerini, M. A. Lazar, SR9009 has REV-ERB-independent effects on cell proliferation and metabolism. *Proc. Natl. Acad. Sci. U.S.A.* **116**, 12147–12152 (2019).
71. E. Bettelli, Y. Carrier, W. Gao, T. Korn, T. B. Strom, M. Oukka, H. L. Weiner, V. K. Kuchroo, Reciprocal developmental pathways for the generation of pathogenic effector TH17 and regulatory T cells. *Nature* **441**, 235–238 (2006).
72. Y. P. Rubtsov, J. P. Rasmussen, E. Y. Chi, J. Fontenot, L. Castelli, X. Ye, P. Treuting, L. Siewe, A. Roers, W. R. Henderson Jr., W. Muller, A. Y. Rudensky, Regulatory T cell-derived interleukin-10 limits inflammation at environmental interfaces. *Immunity* **28**, 546–558 (2008).
73. S. Picelli, O. R. Faridani, Å. K. Björklund, G. Winberg, S. Sagasser, R. Sandberg, Full-length RNA-seq from single cells using Smart-seq2. *Nat. Protoc.* **9**, 171–181 (2014).
74. D. J. McCarthy, Y. Chen, G. K. Smyth, Differential expression analysis of multifactor RNA-Seq experiments with respect to biological variation. *Nucleic Acids Res.* **40**, 4288–4297 (2012).

75. A. Krämer, J. Green, J. Pollard Jr., S. Tugendreich, Causal analysis approaches in Ingenuity Pathway Analysis. *Bioinformatics* **30**, 523–530 (2014).
76. A. Subramanian, P. Tamayo, V. K. Mootha, S. Mukherjee, B. L. Ebert, Gene set enrichment analysis: A knowledge-based approach for interpreting genome-wide expression profiles. *Proceedings of the National Academy of Sciences* **102**, 15545–15550 (2005).
77. E. Y. Chen, C. M. Tan, Y. Kou, Q. Duan, Z. Wang, G. V. Meirelles, N. R. Clark, A. Ma'ayan, Enrichr: Interactive and collaborative HTML5 gene list enrichment analysis tool. *BMC. Bioinformatics* **14**, 128 (2013).
78. M. V. Kuleshov, M. R. Jones, A. D. Rouillard, N. F. Fernandez, Q. Duan, Z. Wang, S. Koplev, S. L. Jenkins, K. M. Jagodnik, A. Lachmann, M. G. McDermott, C. D. Monteiro, G. W. Gundersen, A. Ma'ayan, Enrichr: A comprehensive gene set enrichment analysis web server 2016 update. *Nucleic Acids Res.* **44**, W90–W97 (2016).
79. T. Stuart, A. Butler, P. Hoffman, C. Hafemeister, E. Papalexi, W. M. Mauck III, Y. Hao, M. Stoeckius, P. Smibert, R. Satija, Comprehensive integration of single-cell data. *Cell* **177**, 1888–1902.e21 (2019).
80. P. Baskaran, B. Thyagarajan, Measurement of basal and forskolin-stimulated lipolysis in inguinal adipose fat pads. *J. Vis. Exp.* , 55625 (2017).
81. M. E. Hughes, J. B. Hogenesch, K. Kornacker, JTK_CYCLE: An efficient nonparametric algorithm for detecting rhythmic components in genome-scale data sets. *J. Biol. Rhythms* **25**, 372–380 (2010).

Acknowledgments: We thank Y. Chen, A. Baysoy, K. Seddu, A. Cook, B. Vijaykumar, L. Yang, K. Hattori, A. Ortiz-Lopez, N. Asinovski, F. Chen, G. Buruzula, A. Wood, C. Araneo, F. Lopez, D. Ischiu, B. Hanna, and M. Marin-Rodero for experimental assistance; C. Laplace for graphics; and B. Spiegelman and his laboratory for helpful advice. Cell sorting was supported by the Flow Cytometry Core of NIH P30 DK036836 and by the Harvard Medical School Flow Cytometry Core. **Funding:** This work was supported by the following grants and fellowships: NIH DK092541, NIH RC2DK116691, and the JPB Foundation to D.M.; the JPB Foundation and NIH DK45586 to M.L.; and NIH F32AG072874 to P.K.L. and T32GM007753 for T.J. **Author contributions:** This work was conceptualized by T.X., P.K.L., and D.M.; T.X., P.K.L., A.R.M.-R., and T.J. developed methods, performed experiments, and analyzed data. M.A.L. provided key materials. T.X., P.K.L., A.R.M.-R., and D.M. wrote the original manuscript, which was edited by all authors. This project was supervised by D.M. and C.B., and funding was acquired by D.M. and M.A.L. **Competing interests:** The authors declare that they have no competing interests. **Data and materials availability:** Population-level RNA-seq between genotypes (GSE206775) and over circadian time (GSE206774), RNA-seq of whole VAT (GSE206776), and scRNA-seq (GSE206949) datasets have been deposited in Gene Expression Omnibus. All data needed to evaluate the conclusions in the paper are present in the paper or the Supplementary Materials.

Submitted 3 August 2021
Resubmitted 30 June 2022
Accepted 19 August 2022
Published 30 September 2022
10.1126/sciimmunol.abl7641

Science Immunology

T_{regs} in visceral adipose tissue up-regulate circadian-clock expression to promote fitness and enforce a diurnal rhythm of lipolysis

Tianli Xiao, P. Kent Langston, Andrés R. Muñoz-Rojas, Teshika Jayewickreme, Mitchell A. Lazar, Christophe Benoist, and Diane Mathis

Sci. Immunol., **7** (75), eabl7641.
DOI: 10.1126/sciimmunol.abl7641

Bedtime for T_{regs}

Regulatory T cells (T_{regs}) in visceral adipose tissue (VAT) are key to regulating local and systemic metabolism. Circadian rhythm pathways are up-regulated in tissue-T_{regs}, yet it is unclear how they affect VAT T_{regs}. Here, Xiao *et al.* determined the transcriptomic and metabolic profiles of VAT T_{regs} at various circadian time points in mice that expressed or were deficient in expression of core-clock genes (genes that control circadian rhythms). VAT T_{regs} had altered phenotypes at various times during the circadian cycle and ablation of *Bmal1*, a core clock gene, which led to VAT T_{reg} constitutive activation and altered metabolism, fitness loss, and the greater suppression of adipocyte lipolysis. Thus, diurnal rhythm plays a key role in the function and regulation of VAT T_{regs}.

Science Immunology (ISSN) is published by the American Association for the Advancement of Science. 1200 New York Avenue NW, Washington, DC 20005. The title *Science Immunology* is a registered trademark of AAAS.